REPORT DOCUMENTATION PAGE

Form Approved OMB NO. 0704-0188

The public reporting burden for this collection of information is estimated to average 1 hour per response, including the time for reviewing instructions, searching existing data sources, gathering and maintaining the data needed, and completing and reviewing the collection of information. Send comments regarding this burden estimate or any other aspect of this collection of information, including suggesstions for reducing this burden, to Washington Headquarters Services, Directorate for Information Operations and Reports, 1215 Jefferson Davis Highway, Suite 1204, Arlington VA, 22202-4302. Respondents should be aware that notwithstanding any other provision of law, no person shall be subject to any oenalty for failing to comply with a collection of information if it does not display a currently valid OMB control number.
PLEASE DO NOT RETURN YOUR FORM TO THE ABOVE ADDRESS.

1. REPORT DATE (DD-MM-YYYY)	2. REPORT TYPE	3. DATES COVERED (From - To)
17-09-2012	Final Report	1-Oct-2011 - 30-Jun-2012

4. TITLE AND SUBTITLE	5a. CONTRACT NUMBER
"Ductilization of High-Strength Magnesium Alloys"	W911NF-11-1-0539
	5b. GRANT NUMBER
	5c. PROGRAM ELEMENT NUMBER
	611102

6. AUTHORS	5d. PROJECT NUMBER
Gregory B. Olson, Shengjun (Dennis) Zhang	
	5e. TASK NUMBER
	5f. WORK UNIT NUMBER

7. PERFORMING ORGANIZATION NAMES AND ADDRESSES	8. PERFORMING ORGANIZATION REPORT NUMBER
Northwestern University Evanston Campus Office for Sponsored Research (OSR) 1801 Maple Ave., Suite 2410 Evanston, IL 60201 -	

9. SPONSORING/MONITORING AGENCY NAME(S) AND ADDRESS(ES)	10. SPONSOR/MONITOR'S ACRONYM(S)
U.S. Army Research Office P.O. Box 12211 Research Triangle Park, NC 27709-2211	ARO
	11. SPONSOR/MONITOR'S REPORT NUMBER(S)
	61350-MS-II.1

12. DISTRIBUTION AVAILIBILITY STATEMENT

Approved for Public Release; Distribution Unlimited

13. SUPPLEMENTARY NOTES

The views, opinions and/or findings contained in this report are those of the author(s) and should not contrued as an official Department of the Army position, policy or decision, unless so designated by other documentation.

14. ABSTRACT

A computational materials design approach is extended to high-strength Magnesium alloys to predict new compositions and novel multistep thermal processing to enhance ductility. Design modeling employing highly precise FLAPW all-electron DFT quantum mechanical calculations focus on the enhancement of grain boundary cohesion, based on the Rice-Wang thermodynamic model previously validated in high-performance steels. The calculations identify the cohesion enhancing potencies of grain boundary segregants as well as the segregation

15. SUBJECT TERMS

Materials genome, materials design

16. SECURITY CLASSIFICATION OF:			17. LIMITATION OF ABSTRACT	15. NUMBER OF PAGES	19a. NAME OF RESPONSIBLE PERSON
a. REPORT	b. ABSTRACT	c. THIS PAGE			Gregory Olson
UU	UU	UU	UU		19b. TELEPHONE NUMBER
					847-491-5222

Standard Form 298 (Rev 8/98)
Prescribed by ANSI Std. Z39.18

Report Title

"Ductilization of High-Strength Magnesium Alloys"

ABSTRACT

A computational materials design approach is extended to high-strength Magnesium alloys to predict new compositions and novel multistep thermal processing to enhance ductility. Design modeling employing highly precise FLAPW all-electron DFT quantum mechanical calculations focus on the enhancement of grain boundary cohesion, based on the Rice-Wang thermodynamic model previously validated in high-performance steels. The calculations identify the cohesion enhancing potencies of grain boundary segregants as well as the segregation energies controlling grain boundary composition. The predicted surface thermodynamic parameters are integrated with bulk thermodynamics to predict novel alloy compositions and new thermal processing to optimize grain boundary composition in precipitation-strengthened alloys with enhanced ductility.

Enter List of papers submitted or published that acknowledge ARO support from the start of the project to the date of this printing. List the papers, including journal references, in the following categories:

(a) Papers published in peer-reviewed journals (N/A for none)

Received   Paper

TOTAL:

Number of Papers published in peer-reviewed journals:

(b) Papers published in non-peer-reviewed journals (N/A for none)

Received   Paper

TOTAL:

Number of Papers published in non peer-reviewed journals:

(c) Presentations

Number of Presentations: 0.00

Non Peer-Reviewed Conference Proceeding publications (other than abstracts):

<u>Received</u> <u>Paper</u>

TOTAL:

Number of Non Peer-Reviewed Conference Proceeding publications (other than abstracts):

Peer-Reviewed Conference Proceeding publications (other than abstracts):

<u>Received</u> <u>Paper</u>

TOTAL:

Number of Peer-Reviewed Conference Proceeding publications (other than abstracts):

(d) Manuscripts

<u>Received</u> <u>Paper</u>

TOTAL:

Number of Manuscripts:

Books

<u>Received</u> <u>Paper</u>

TOTAL:

Patents Submitted

Patents Awarded

Awards

Gregory B. Olson elected to American Academy of Arts & Sciences

Graduate Students

NAME	PERCENT SUPPORTED
FTE Equivalent:	
Total Number:	

Names of Post Doctorates

NAME	PERCENT_SUPPORTED
Shengjun (Dennis) Zhang	1.00
FTE Equivalent:	**1.00**
Total Number:	**1**

Names of Faculty Supported

NAME	PERCENT SUPPORTED	National Academy Member
Gregory B. Olson	0.07	Yes
FTE Equivalent:	**0.07**	
Total Number:	**1**	

Names of Under Graduate students supported

NAME	PERCENT_SUPPORTED	Discipline
Jie Han	0.00	Materials Science and Engineering
Yoon Joo Na	0.00	Materials Science and Engineering
Sky Park	0.00	Materials Science and Engineering
FTE Equivalent:	**0.00**	
Total Number:	**3**	

Student Metrics
This section only applies to graduating undergraduates supported by this agreement in this reporting period

The number of undergraduates funded by this agreement who graduated during this period: 0.00

The number of undergraduates funded by this agreement who graduated during this period with a degree in science, mathematics, engineering, or technology fields:...... 0.00

The number of undergraduates funded by your agreement who graduated during this period and will continue to pursue a graduate or Ph.D. degree in science, mathematics, engineering, or technology fields:...... 0.00

Number of graduating undergraduates who achieved a 3.5 GPA to 4.0 (4.0 max scale): 0.00

Number of graduating undergraduates funded by a DoD funded Center of Excellence grant for Education, Research and Engineering:...... 0.00

The number of undergraduates funded by your agreement who graduated during this period and intend to work for the Department of Defense 0.00

The number of undergraduates funded by your agreement who graduated during this period and will receive scholarships or fellowships for further studies in science, mathematics, engineering or technology fields: 0.00

Names of Personnel receiving masters degrees

NAME

Total Number:

Names of personnel receiving PHDs

NAME

Total Number:

Names of other research staff

NAME   PERCENT_SUPPORTED

FTE Equivalent:
Total Number:

Sub Contractors (DD882)

Inventions (DD882)

Scientific Progress

Please see attachment

Technology Transfer

ARO STIR Project Final Report

Grant # W911NF-11-1-0539

"Ductilization of High-Strength Magnesium Alloys"

Principal Investigator: Prof. G. B. Olson, Northwestern University

BAA Topic 15.3 Synthesis and Processing of Materials

TPOC: Dr. Suveen Mathaudhu, ARO

Table of Contents

Abstract: A computational materials design approach is extended to high-strength Magnesium alloys to predict new compositions and novel multistep thermal processing to enhance ductility. Design modeling employing highly precise FLAPW all-electron DFT quantum mechanical calculations focus on the enhancement of grain boundary cohesion, based on the Rice-Wang thermodynamic model previously validated in high-performance steels. The calculations identify the cohesion enhancing potencies of grain boundary segregants as well as the segregation energies controlling grain boundary composition. The predicted surface thermodynamic parameters are integrated with bulk thermodynamics to predict novel alloy compositions and new thermal processing to optimize grain boundary composition in precipitation-strengthened alloys with enhanced ductility.

Background

A feasibility demonstration of application of our materials design approach [Olson 1997, Olson 2000] to high-strength Magnesium alloys was previously conducted under ARL support [Olson 2010]. Summarized by the system chart of Figure 1, a range of precipitation strengthening mechanisms has been investigated with particular attention to fundamental metrics operating in the Zr grain-refined Mg-Y-Nd WE43 alloy. Figure 2 shows a LEAP tomographic reconstruction and measured composition profile across nanoscale precipitates in the peak hardness condition providing phase relation data supporting further composition optimization for enhanced strengthening. All-electron FLAPW DFT quantum mechanical calculations of the ideal Griffith work of fracture summarized in Figure 3 predict a lower work of fracture for cleavage on the basal plane vs. the prism plane, and predict that Y in solution has a large beneficial effect in increasing the work of basal plane fracture. This suggests the matrix Y content measured in Figure 2 is a significant factor contributing to the balance of strength and ductility in this system. Figure 4 compares true stress strain curves measured for the solution-treated and peak-aged conditions. Fractography of the latter gives the surprising result that intergranular fracture is the dominant failure mode despite good fracture ductility. This indicates an opportunity to achieve greater strength/ductility combinations in this system by application of our previously validated surface thermodynamic approach to GB cohesion enhancement.

Figure 5 summarizes the core of our approach, as previously demonstrated in high-strength steels. The engineering quantity of interest is the measured embrittlement potency of intergranular segregants as quantified by the intergranular DBTT temperature shift per amount of GB segregant. As an early activity of our SRG materials design consortium [Olson 1997], the Rice-Wang thermodynamic model of interfacial embrittlement [Rice-Wang 1989] predicted this quantity will scale with the difference between the segregation energies of the component in the free surface and GB environments. Predicting this energy difference with FLAPW quantum mechanical calculations then gave the strong correlation of Figure 5 for the well-studied cases of B, C, P and S with and without the prior GB segregation of Mn. With this degree of fundamental model validation, a simplified model was derived from the FLAPW results to predict the behavior of substitutional alloying elements summarized in Figure 6 [Geng et al 2001], followed by rigorous confirmation by detailed FLAPW calculations of the most promising alloying components for GB cohesion enhancement. Building a surface thermodynamic database in this way supported the design of steels such as Ferrium S53 [Kuehmann-Olson 2010] which are immune to intergranular failure.
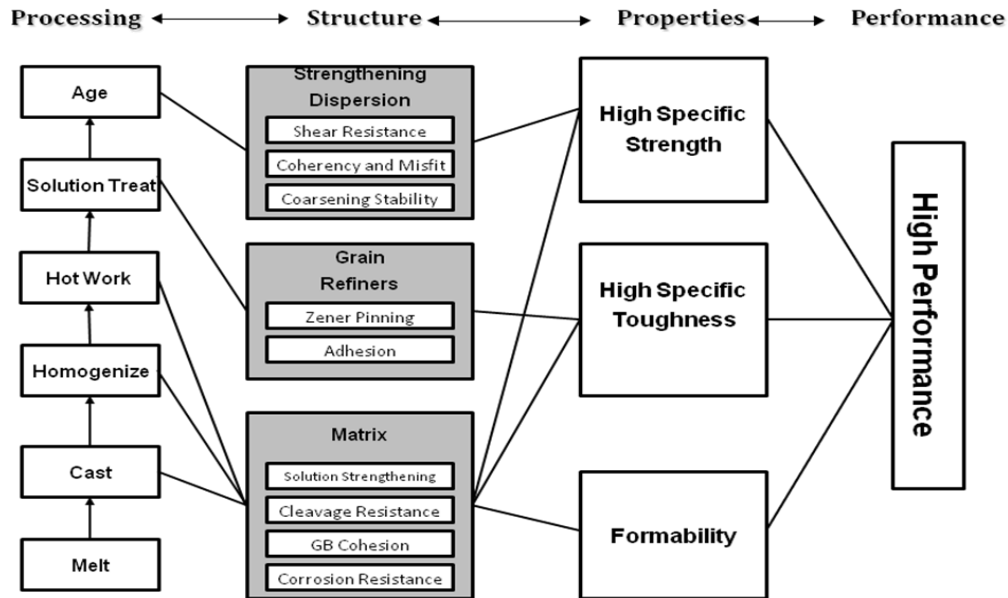
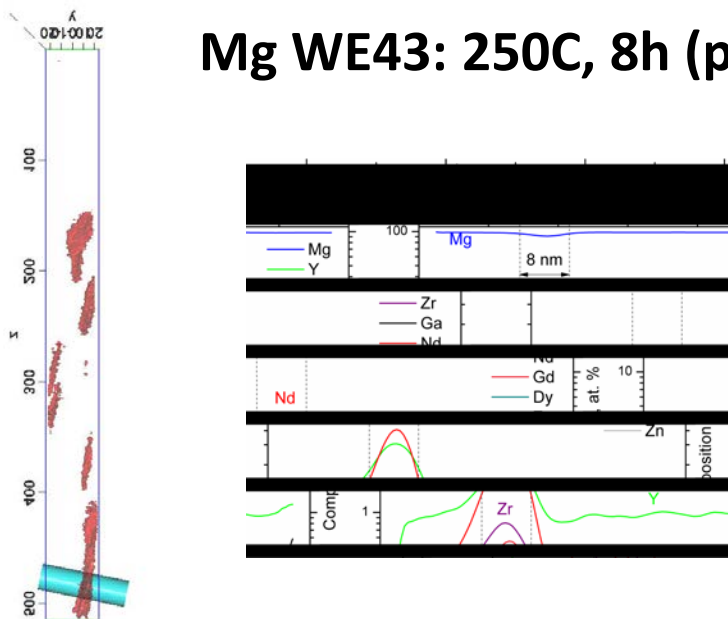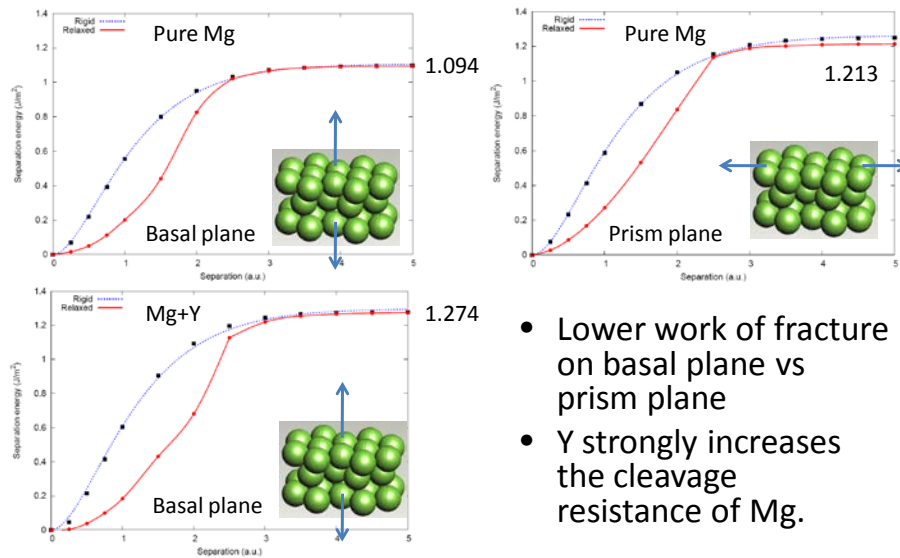Figure 1. Design System Chart for High-Performance Mg-based Alloy

Figure 2. LEAP tomographic atom-probe reconstruction and microanalysis of nanoscale strengthening precipitates in WE43 Mg alloy at peak hardness

- Lower work of fracture on basal plane vs prism plane
- Y strongly increases the cleavage resistance of Mg.

Figure 3. FLAPW calculation of ideal cleavage fracture work in Mg with and without Y
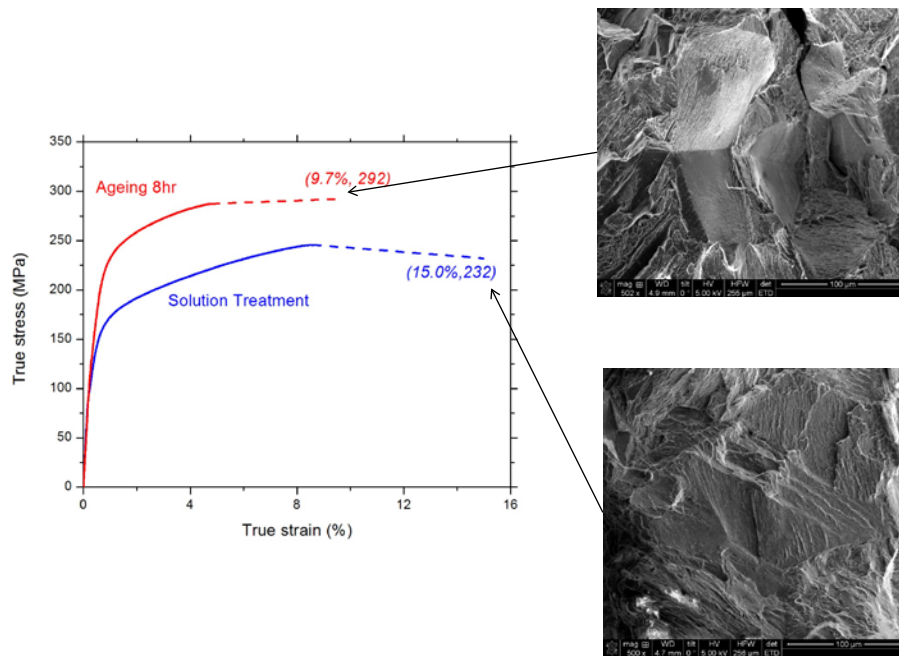
Figure 4. Measured true stress-strain curves and fractography of WE43 Mg alloy

Grain Boundary Embrittlement

Embrittlement Sensitivity
(K/at. %)

ΔE (kJ/mol)
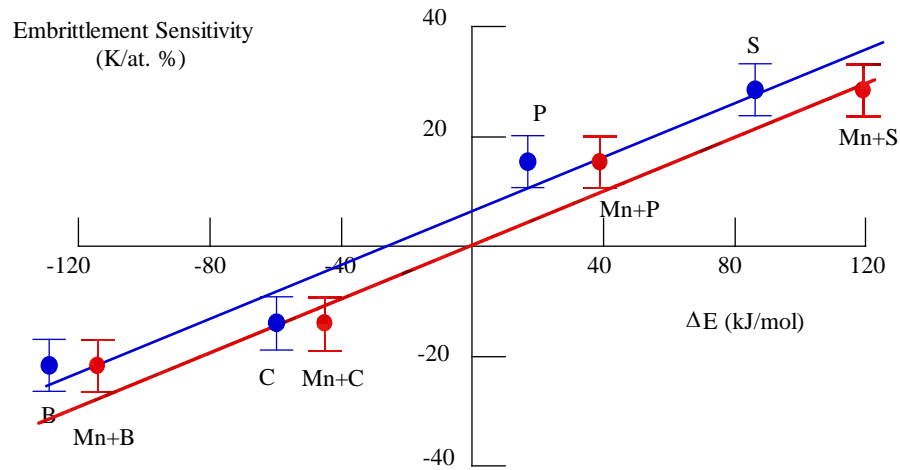
J.R. Rice and J.-S. Wang, Mater. Sci. Eng., 1988

Figure 5. Validated correlation of measured grain boundary embrittlement potency in steels with calculated surface thermodynamic metric of the Rice-Wang model
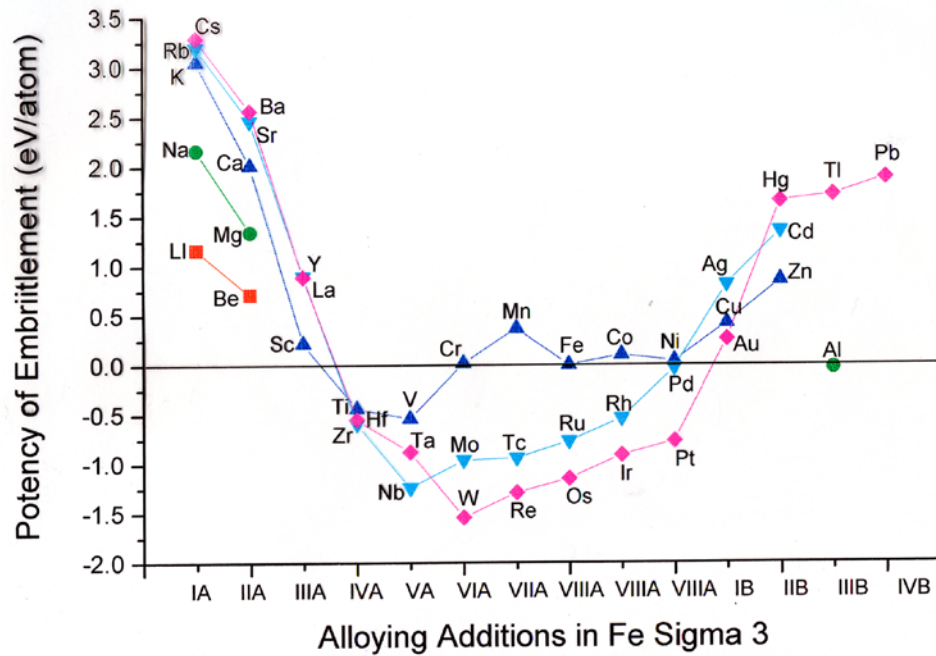
Figure 6. Predicted surface thermodynamic database for embrittlement potency of substitutional segregants in steels

Research Approach

Application to Mg alloys of the ductilization approach previously validated in steels initially employed the simple Sigma7 HCP tilt boundary of Figure 7 (viewed along the HCP "c" axis) as a computational testbed. This computationally efficient short-period, high-symmetry boundary was selected for its non-special character as a high-energy, high free-volume boundary of the type most susceptible to fracture. Highly precise all-electron DFT quantum mechanical calculations are applied to compute the energy difference of boundary segregants in the grain boundary (GB) and corresponding free surface (FS) environments. As in the example of Figure 6, substitutional alloying elements are placed in the site labeled as "A1" in Figure 7, for both the GB and FS environments. As in Figure 5, it is this energy difference per atom that defines an element's embrittlement or cohesion enhancement potency by the Rice-Wang thermodynamic theory. Such calculations identify desirable components to bring to the grain boundary. Once these are identified, calculation of the energy difference between the GB and crystal sites away from the GB defines the GB segregation energy supporting predictive thermal process optimization to enhance the concentration of desired cohesion enhancers at the GB.

In support of feasibility of this approach, a team of students in a Materials Design class project during the 2011 Spring Quarter [Chen et al 2011] applied simpler pseudopotential-based DFT calculations employing the VASP code to the boundary of Figure 7, predicting the atomic potencies summarized in Table 1. Here positive values denote embrittlement while negative values denote cohesion enhancement. Of the initial alloying elements surveyed, Zr and Nb stand out as potentially very effective GB cohesion enhancers if they can be made to segregate to the GB. The computed GB segregation energies summarized in Table 2 indicate a significantly negative (favoring segregation) energy for both Zr and Nb. These initial estimates suggested that the same phenomena exploited in computational design of high-strength steels are available to enhance GB-fracture-limited ductility in Mg alloys.

Building on these estimates, our recent research has applied the much more accurate all-electron FLAPW method to the alloying elements of Table 1, addressing both GB cohesion potency and GB segregation energy. The initial set of calculations was used to calibrate a simple model of the type represented in Figure 6 to identify further desirable alloying candidates. Such projections motivated rigorous FLAPW calculations of desirable candidates. As in the example of high-performance steels, the resulting surface thermodynamic database are combined with available bulk thermodynamics in the design of new alloy compositions and novel multistep thermal processing optimized for enhancement of ductility through greatly increased GB cohesion.

Design integration by a Materials Design class team in Spring 2012 identified new directions in efficient precipitation strengthening and grain refinement in such Mg alloys, aided by the bulk thermodynamic and mobility databases developed based on our previous research.
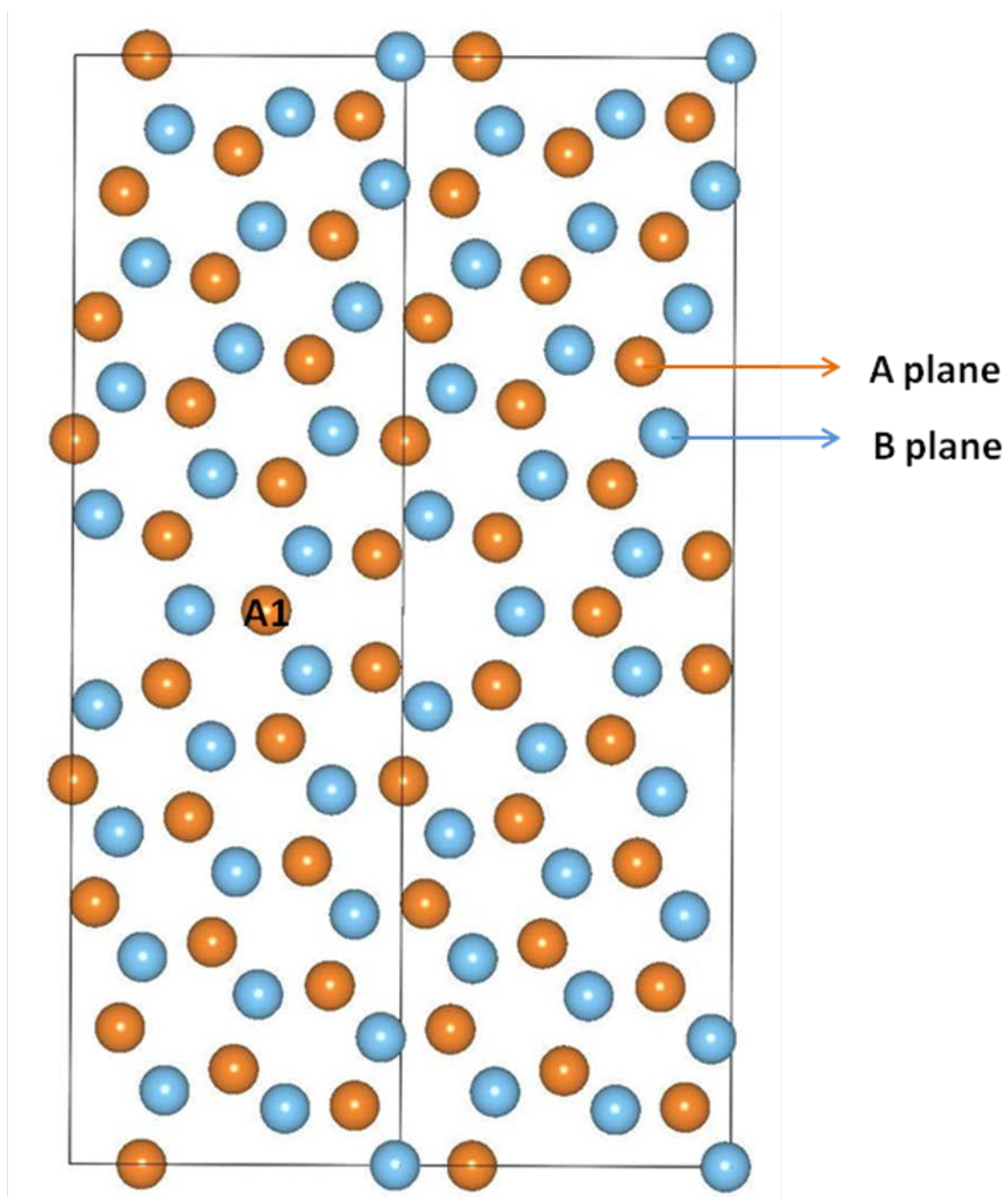
Figure 7. Sigma7 HCP tilt boundary viewed along HCP "c" tilt axis, with A and B basal planes denoted. Substitutional alloying element GB core site is denoted as A1.

Table 1 – Preliminary Pseudopotential DFT Calculated Embrittlement/Cohesion Potencies in HCP Mg.

Solute	GB Embrittlement Potency (eV/atom)
Li	0.30
Na	0.95
Al	-0.12
Zn	0.13
Y	-0.71
Zr	-1.70
Nb	-2.13
Nd	-0.46

Table 2 – Preliminary Pseudopotential DFT Calculated GB Segregation Energies in HCP Mg.

Solute	GB Segregation Energy (eV/atom)
Li	0.00
Na	0.00
Al	-0.01
Zn	0.00
Y	-0.07
Zr	-0.13
Nb	-0.17

Research Results

(a) FLAPW Calculations

For the rigorous FLAPW calculations, the symmetrical tilt Mg $\Sigma 7(12\bar{3}0)[0001]$ was further refined. Figure 8 represents the refined structure of the GB model employed. From the basis of the HCP crystal structure, the A and B type basal planes correspond to distinct boundary sites we denote as Types I and II respectively.
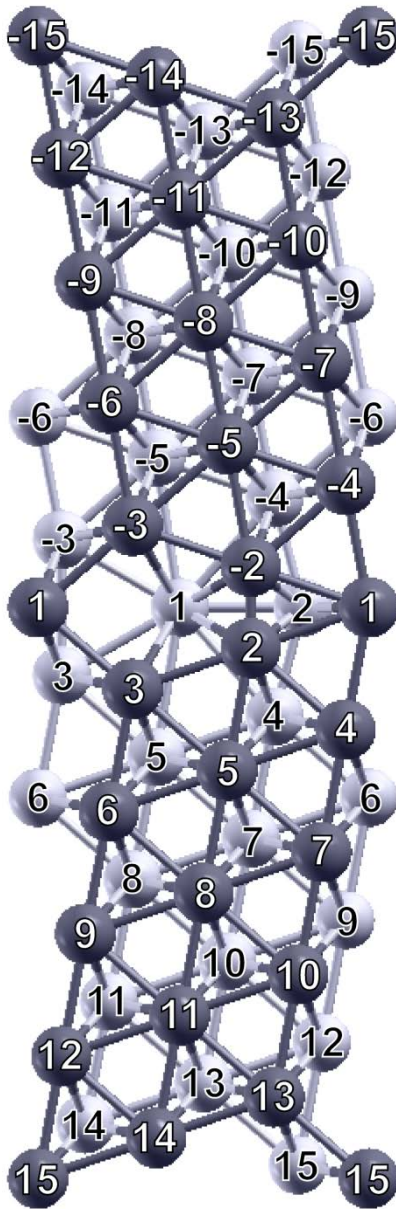
Fig. 8. . Crystal structures of the Mg $\sum 7(12\bar{3}0)[0001]$ GB. The dark grey and light grey atoms represent atoms in layers with *y*=0 (in the paper plane) and *y*=0.5 (beneath the paper plane) along the [0001] direction, respectively. Site 1 is on the mirror plane; Sites *i* and –*i* (*i* =2 to15) have mirror symmetry.

As described earlier, the embrittlement potency concept is based on the thermodynamic theory by Rice and Wang which describes the mechanism of intergranular embrittlement through a competition between plastic crack blunting and brittle boundary separation. The term "embrittlement potency"

refers to a change of grain-boundary adhesion energy induced by the segregant species, and, according to the Rice-Wang model, its quantity is defined as:

$$\Delta E = (E_{GB}^M - E_{GB}) - (E_{FS}^M - E_{FS})$$

where E_{GB}, E_{GB}^M, E_{FS}, $and\ E_{FS}^M$ are the total energies of clean and impurity-segregated GB, and clean and impurity-adsorbed FS, respectively. First-principles calculations conducted here by Dr. Dennis Zhang have used both the Rice-Wang model and the ab initio computational tensile test. The highly precise all-electron full-potential linearized augmented plane-wave (FLAPW) method was employed. Figure 9 depicts the fully converged computed charge densities for the pure Mg boundary, showing the distinct character of the I and II planes. In contrast to our previous work on Fe and Al based systems, the Mg boundaries proved difficult to converge in the all-electron calculations, limiting the number of components that could be evaluated in the course of this project. Nonetheless, Table 3 summarizes the computed potencies of the segregants Na, Y, Al, Zn, and Li. Of these, Na is the most potent embrittler, and Y is predicted to be a significant cohesion enhancer. Details of the Na behavior are summarized in Figure 10, showing that Na favors the largest free volume site, type II-1, imposing an additional boundary expansion, with a boundary segregation energy of 0.44 eV/atom. The example of the strongly cohesion enhancing Y is shown in Figure 11, where the segregant also prefers the II-1 site with a very significant segregation energy of 0.84 eV/atom and a cohesion enhancement potency of 0.93 eV/atom. Clearly, optimization of alloy composition to maximize grain boundary Y content offers a high potential for improving boundary cohesion to suppress the intergranular fracture that currently limits ductility.
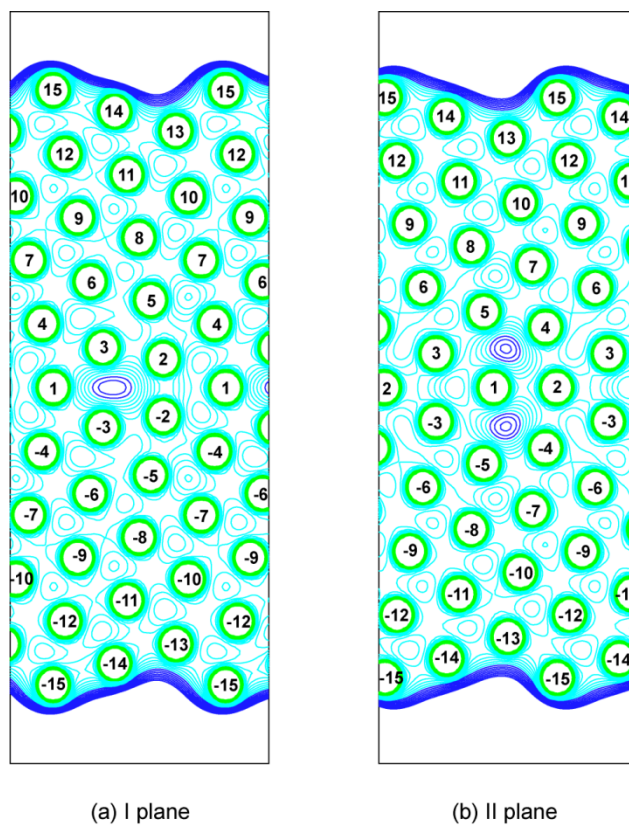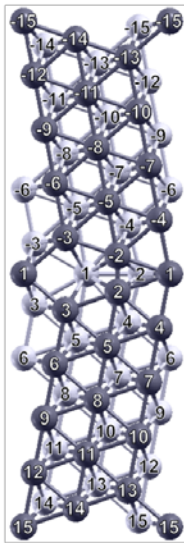
(a) I plane   (b) II plane

Fig. 9. Calculated charge density for pure Mg GB.

Table 3. FLAPW Calculated Embrittlement Potency

Solute Atom	GB Embrittlement Potency (eV/atom)
Na	0.238
Y	-0.835
Al	-0.233
Zn	-0.202
Li	0.128

Na in Mg GB

Position	Cell expansion	Segregation energy eV/atom
I-(8)	0.10	
I-1	0.05	-0.122
I-2	0.00	-0.027
I-3	0.00	-0.215
II-1	0.20	-0.443
II-2	-0.10	0.014
II-3	-0.05	-0.088

(a) I plane (b) II plane
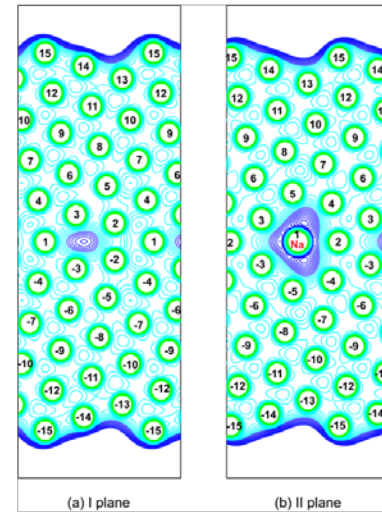
- *Na is an undesired impurity element in Mg alloys and its solubility in hcp Mg is very low*
- *Trace amounts of Na can drastically reduce the strength of Mg*
- Large Na atom segregates into the loosest site II-1 energetically
- Calculated embrittling potency is +0.238 eV/atom which indicates that Na is an embrittler
- Calculated fracture energy is 1.120 eV/atom < 1.207 eV/atom for clean Mg GB
- Inserting a Na atom in II-2 site reduces the charge density significantly , which can be attributed to the less number of Na valence electrons, electron transfer from Na, and the expansion of the structure by the large Na atomic size.

Figure 10. Computed charge densities and segregation energies for Na in Mg grain boundary.

Figure 11. Computed charge densities and segregation energies for Y in Mg grain boundary.

(b) Design Integration

Under the supervision of Dr. Dennis Zhang, a team of students in the Spring 2012 Materials design class integrated the new FLAPW calculations with our previous research and performed the integrated design of a higher-strength Mg alloys optimized for enhanced intergranular cohesion. Their full report is presented here as an Appendix.

The rigorous calculations of Table 3 were employed to calibrate a modified form of the Geng model. The model was then employed to estimate embrittlement potency values for elements whose DFT calculations were not available. As summarized in Figure 12, group 5 and 6 elements have the most negative potency values. It was concluded that the following elements are good cohesion enhancers: Ti, Y, Zr, Nb, Mo, Ru, Hf, Ta, W, and Re.

 Using the McLean segregation model, yttrium and zirconium are predicted to strongly segregate to the grain boundary and contribute to the grain boundary cohesion significantly.

According to our previous atom probe data, the precipitate phase fraction of WE43 at peak hardness is 1.65%, and a calibrated strengthening model gives $\sigma_y = 178 + 475\,f^{1/2}$ for peak yield strength in MPa.

Retaining Zr as a grain refiner that also enhances grain boundary cohesion, the composition corresponding to maximal yttrium solubility for further boundary cohesion enhancement is 1.43 at% Y and 0.54 at% Nd, with solubility at a solution temperature of 820K. Its yield strength is 248MPa, offering a significant increment over WE43, as summarized in Figure 13. Relative to the current WE43 aging temperature of 250°C, longer time aging at lower temperature can increase the precipitate phase fraction for further strength increase.
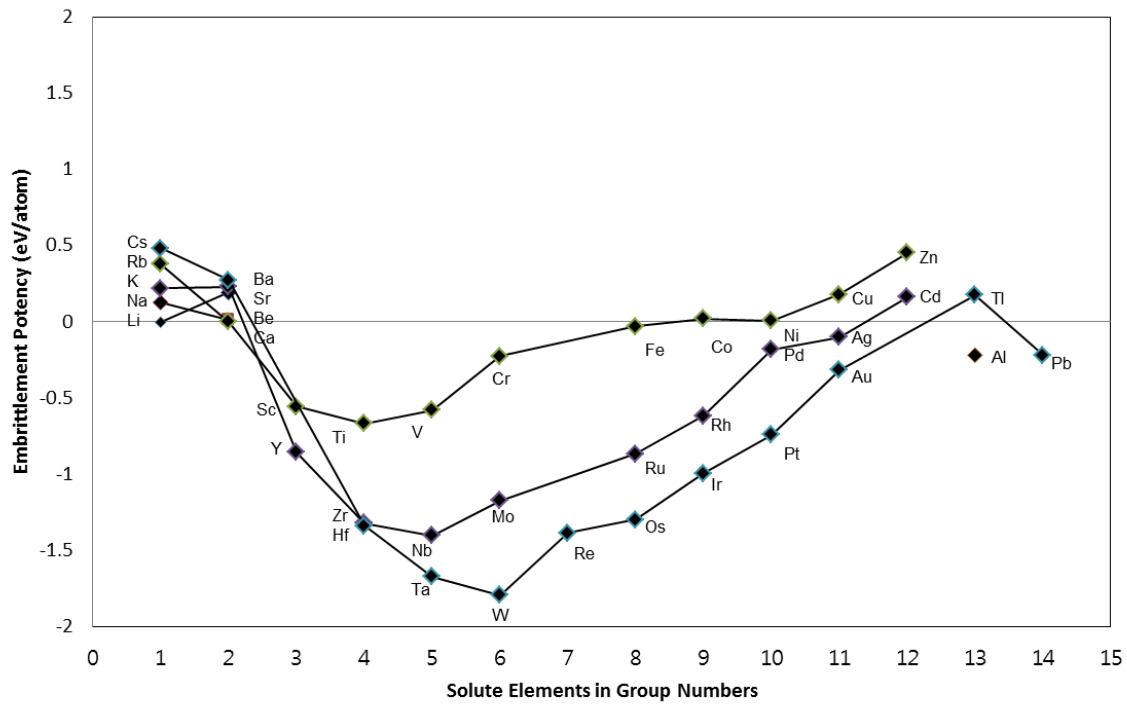
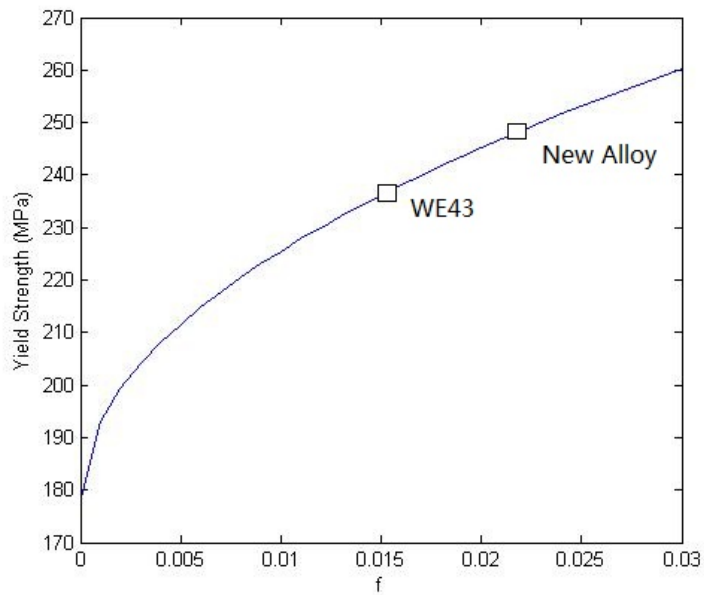Figure 12. Embrittlement Potency Prediction in Magnesium System

Figure 13. Predicted strength increase for designed alloy.

References

[Chen et al 2011] Michelle Chen, Art Counts, Jeff Doak, High Performance Magnesium Alloy, MSc 390 Materials Design project final report, June 4, 2011.

[Geng et al 2001] W.T. Geng, A.J. Freeman, G.B. Olson, Physical Review B 63, 165415 (2001).

[Kuehmann-Olson 2009] C. J. Kuehmann, G. B. Olson, "Computational Materials Design and Engineering," *Materials Science & Technology,* vol 25, no. 4, 2009.

[Olson 1997] G. B. Olson, "Computational Design of Hierarchically Structured Materials," *Science*, Vol. 277, No. 5330 (1997) pp. 1237-1242.

[Olson 2000] G. B. Olson, "Designing a New Material World," *Science* (Millennial Essay) Vol. 288, 12 May 2000, pp. 993-998.

[Olson 2010] G. B. Olson, "Computational Materials Design: Lightweight Alloys," Army Sagamore Research Conference on Lightweight Metals, St. Michaels, MD, June 15, 2010.

[Rice-Wang 1989] J. Rice, J. Wang, Materials Science and Engineering: A 107 (1989) 23-40.

Appendix

High Performance Magnesium Alloy

Final Report

MSE 390

Spring 2012

Advisor:

Dr. Shengjun (Dennis) Zhang

Team Members:

Yoon Joo Na

Sky Park

Jie Han

Table of Contents

1   Background

Magnesium alloys have become very popular in aerospace and automotive industry due to several outstanding properties. Magnesium alloys are very light weight with low density, only two thirds that of aluminum alloys. Magnesium alloys also have good high temperature mechanical properties as well as good corrosion resistance, which make them attractive for aerospace applications, motor racing and other automotive applications. Their light weight provides significant advantages as structural materials for race cars. Other applications include high performance bicycles, electronics, nuclear applications, sporting goods, and office equipment. Recently, dramatic improvements on superior corrosion resistance have been achieved. For these reasons, many users and designers are looking for further alloy development on improving other mechanical properties. In the 2007 Triennial International Aircraft Fire & Cabin Safety Research Conference, Magnesium Elektron Company projected a steady increase in world automotive demand for magnesium die castings. The increasing trend since 1991 to 2010 is illustrated by Figure 1 below.
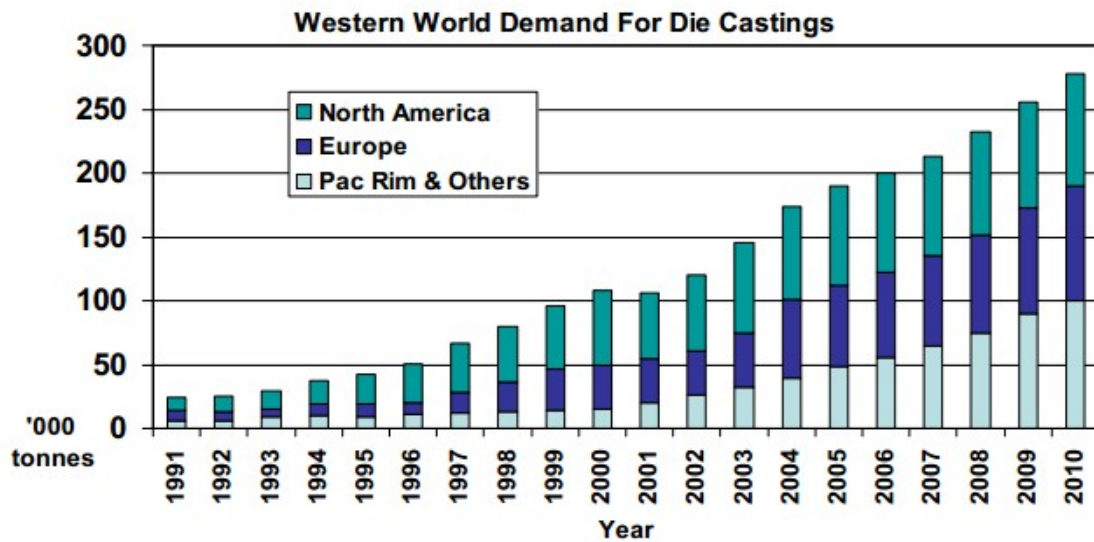
Figure 1 Forecasted Demand for Magnesium Die Castings

RZ5, ZRE1, MSR, and EQ21 alloys have been widely used for aircraft engines and gearbox casings for many years. The current state-of-art cast magnesium alloys, however, have been reported to be magnesium-rare earth alloys. The rare earth elements have relatively high solubility in magnesium, and it decreases with decreasing temperature, which makes age hardening possible. Compared with older magnesium alloys, Mg-RE alloys enjoy superior corrosion resistance and high temperature properties.

1.1 WE43 and WE54

Two commercial Mg-RE alloys have been prepared by the MEL Ltd. Company since the late 1980s: WE43 and WE54. Besides Y and Nd, small amount of Zr is added as a grain refinement element. WE alloys are expected to replace former magnesium alloys that were used for aerospace application due to improved corrosion resistance and high temperature properties that make them suitable for working temperature of up to 300°C. Figure 2 exhibits the temperature dependence of strength for WE54, and it shows that up to 250°C, WE54 maintains the 0.2 proof strength of 175 MPa and tensile strength of 230 MPa.

Table 1 lists major properties of WE43 and WE54.
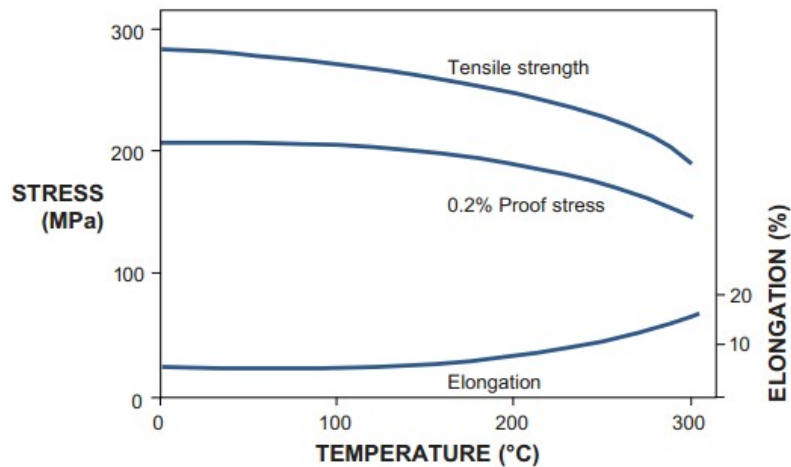
Figure 2 Effect of temperature on tensile properties of WE54 [1]

Table 1 WE43 and WE54 properties at ambient temperature [1]

Alloy	Composition	0.2 % Proof stress	Tensile strength	Elongation	Fracture toughness	Heat treatment
WE43	Mg-4 wt%Y-3.3 wt%RE-0.5wt%Zr	180 MPa	250 MPa	7%	15.9 MPa m$^{1/2}$	solution treat 525℃/8h, age 250℃/16h
WE54	Mg-5.5 wt%Y-2 wt%Nd-2 wt%RE-0.4wt%Zr	205 MPa	280 MPa	4%	14.3 MPa m$^{1/2}$	solution treat 525℃/8h, age 250℃/16h

WE54 has higher strength and hardness compared to WE43. This is explained by dispersion strengthening mechanism. The decomposition sequence in WE alloys has been determined to be α-Mg(hcp)→β''(D0$_{19}$)→β'(cbco)→β$_1$ and β (fcc). The maximum solvus

temperature for β'' has been reported to be below 200°C, thus during the isothermal aging at 250°C, only the dispersed β' and β contribute to the strength and hardness [2-4]. Both β' and β contain yttrium, thus higher solubility of yttrium in solid solution, as in WE54, leads to larger phase fraction of precipitates and, consequently, improved strength.

1.2 WE54 Hardness

According to an article in the Journal of Achievements in Materials and Manufacturing Engineering by A. Kielbus [6], the cast condition of WE54 alloy is around 77HV and did not undergo much change after solution treatment. The chemical composition of WE54 used by Kielbus is in Table 2 below.

Table 2 Kielbus WE54 Composition in Weight Percent

Y	Nd	Zr	Zn	Si	Fe	Mn	Cu	Mg
5.0	1.7	0.55	<0.001	<0.01	0.002	<0.01	<0.01	balance

This composition was solution treated at 525°C for 8 hours, and aging treatments were performed at 250°C from 4 to 96 hours. Kielbus' results are illustrated in Figure 3 below.
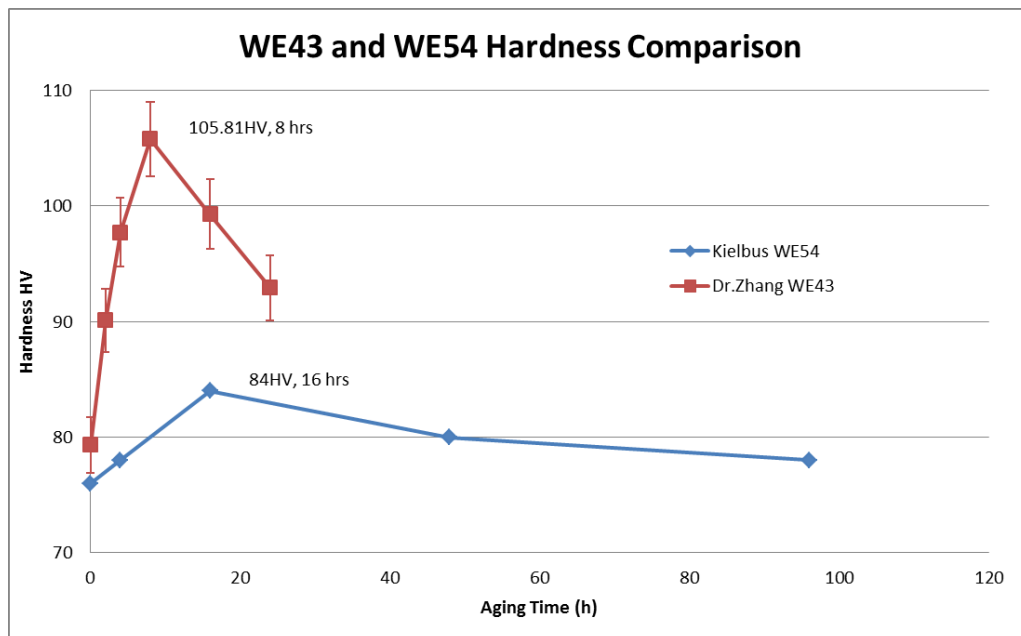

Figure 3 Hardness Comparison of WE43 and WE54 [5]

According to Kielbus' results, the hardness peaked at 84HV with aging time of 16 hours, and further aging decreased the hardness. The varying hardness with respect to aging time is illustrated in Figure 3.

Comparing with Kielbus' WE54 data, Dr. Zhang's 2010 WE43 data show that WE43 responds much more readily to aging. After solution treatment and before aging, WE43 and WE54 have relatively close hardness values of 79 and 76 HV respectively. However, the WE43 responded significantly to aging with peak hardness of 106HV occurring at 8 hours of aging time. In contrast, Kielbus' WE54 only peaked up to 84HV after 16 hours of aging.

Another study done by B. Samola et al in 2011 used WE54T4 and WE54T6 alloys. T4 indicates solution treatment of 525°C for 8 hours, and T6 indicates 200°C for 16 hours. The WE54T4 resulted in hardness of around 70HV, while the T6 alloy had around 107HV (7). From Samola, Kielbus and Dr. Zhang's data, the importance of understanding the optimal solution treatment and aging condition to achieve the maximum hardness possible is apparent.

Table 3 WE54 hardness by B. Samola

Alloy	Solution Treatment	Hardness (HV)
WE54T4	520C/8h	70
WE54T6	200C/16h	107

1.3　Grain Boundary Corrosion and Cleavage Resistance

On the other hand, while both alloys enjoy substantial higher corrosion resistance than common commercial magnesium alloys, WE43 performs better than WE54. Ryzchon et al. [5] reported that with increased exposure time to corrosive solution (3.5% NaCl), the corrosion rate of WE54 increased linearly, while that of WE43 remained almost unchanged, as shown in Figure 4 (left). Further study suggested that the corrosion initiated along grain boundaries Figure 4 (right).
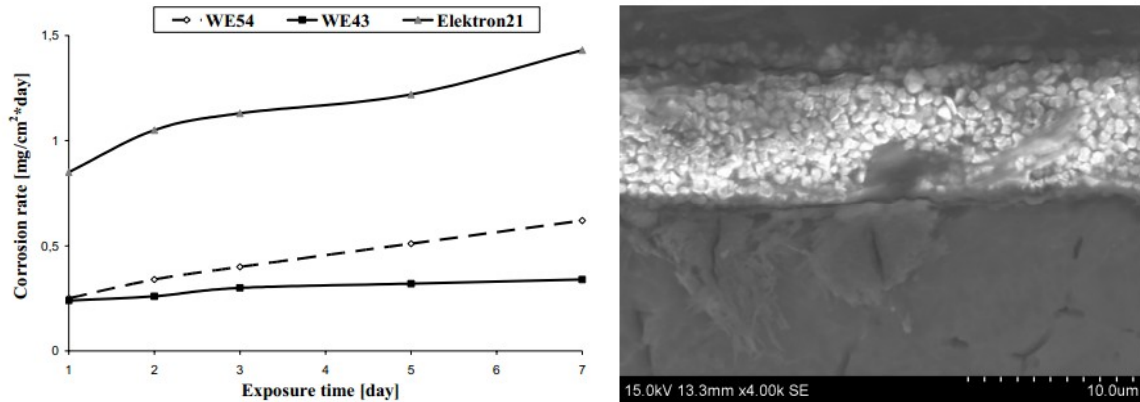
Figure 4 Left: corrosion rates during immersion test of 3.5% NaCl; right: corroded pits along GBs of WE54 [5]

The grain boundary influences fracture toughness as well. Previous work by Zhang exhibited major intergranular fracture in WE43 at peak hardness (Figure 5). WE54 follows similar fracture mechanism. Therefore, the enhancement of grain boundary cohesion plays an important role in the improvement of ductility.
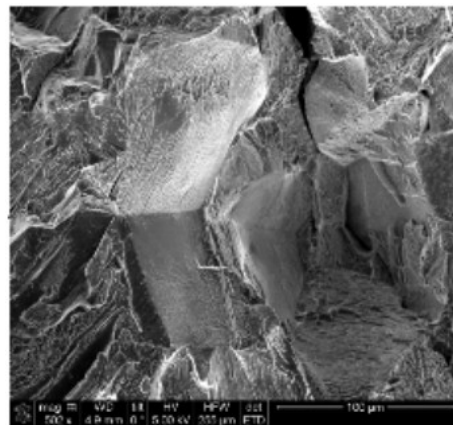
Figure 5 Fractography of WE43 at peak hardness (292 MPa, aging 8h)

Given the information above, in order to achieve higher performance, two substantial factors must be considered: the phase fraction of precipitates and the grain boundary cohesion, and these factors will be the focus of this work.

1.4 Past Work

For the past two decades, Northwestern University has invested in studying high performance magnesium alloys. In particular, Dr. Shengjun Zhang and previous MSE 390 students have been making significant progress in understanding these alloys. In recent years, studies have been done on the commercially available WE43 alloy. Identifying that brittle fracture most often occurs at grain boundaries, Dr. Zhang and his group conducted

computational studies to engineer the structure and composition that can improve fracture toughness by strengthening grain boundaries.

Previous 390 students performed FLAPW and DFT calculations to find grain boundary segregation energy and surface segregation energy to find and calculate the embrittlement potency. The solute atoms that have negative embrittlement potency values are potential cohesion enhancer candidates. In addition, Geng's model [9], which will be discussed in detail later, was used as a phenomenological model and was fitted to DFT calculations in order to estimate the embrittlement potency values for other solute elements. Three requirements must be satisfied in order for a solute atom to successfully strengthen Mg alloy: i) it must be soluble in Mg ii) it must be a cohesion enhancer iii) it must have large grain boundaries segregation energy. Using Dr. Zhang's data and computational calculations, previous 390 students concluded that

- Group 2-5 elements are cohesion enhancers;
- Group 6-13 elements are generally embrittlers in magnesium alloys;
- Cohesion enhancement increases as the rows decreases, i.e., Row 5>Row 4>Row 3;
- Zirconium, in particular, is a potential enhancer that is soluble and has a large GB segregation energy.

They calibrated a strengthening model for the yield strength of WE43 and WE54 as well. Meanwhile, combined Thermocalc calculation with Dr. Zhang's LEAP, TEM, and tensile testing results, the maximal solubility of yttrium was determined and tuned to the strengthening model to estimate the possible improvement in yield strength. Using a solution temperature of 803K and an aging temperature of 523K, $Mg_{98.03}Y_{1.43}Nd_{0.54}$ was proposed to be an optimal composition for strengthening, and its yield strength is predicted to be increased by 317.86MPa, which is 63.8% from 2010's model.
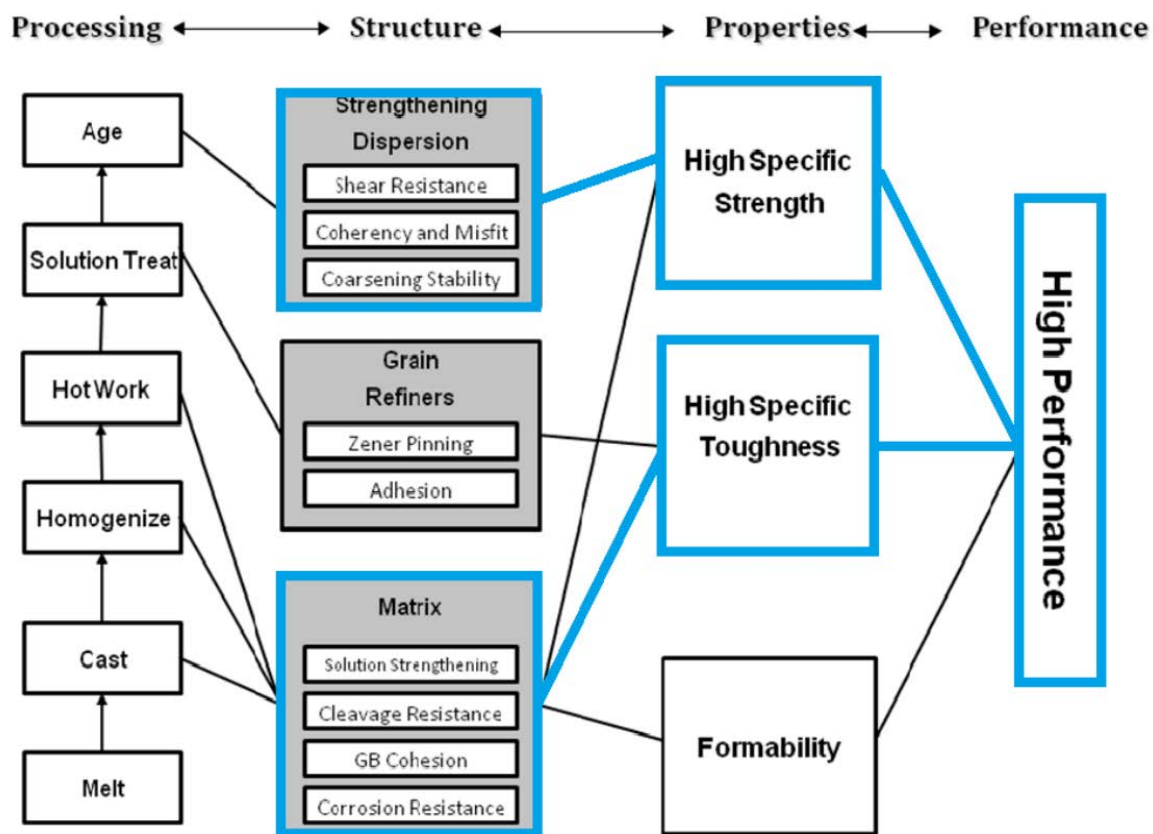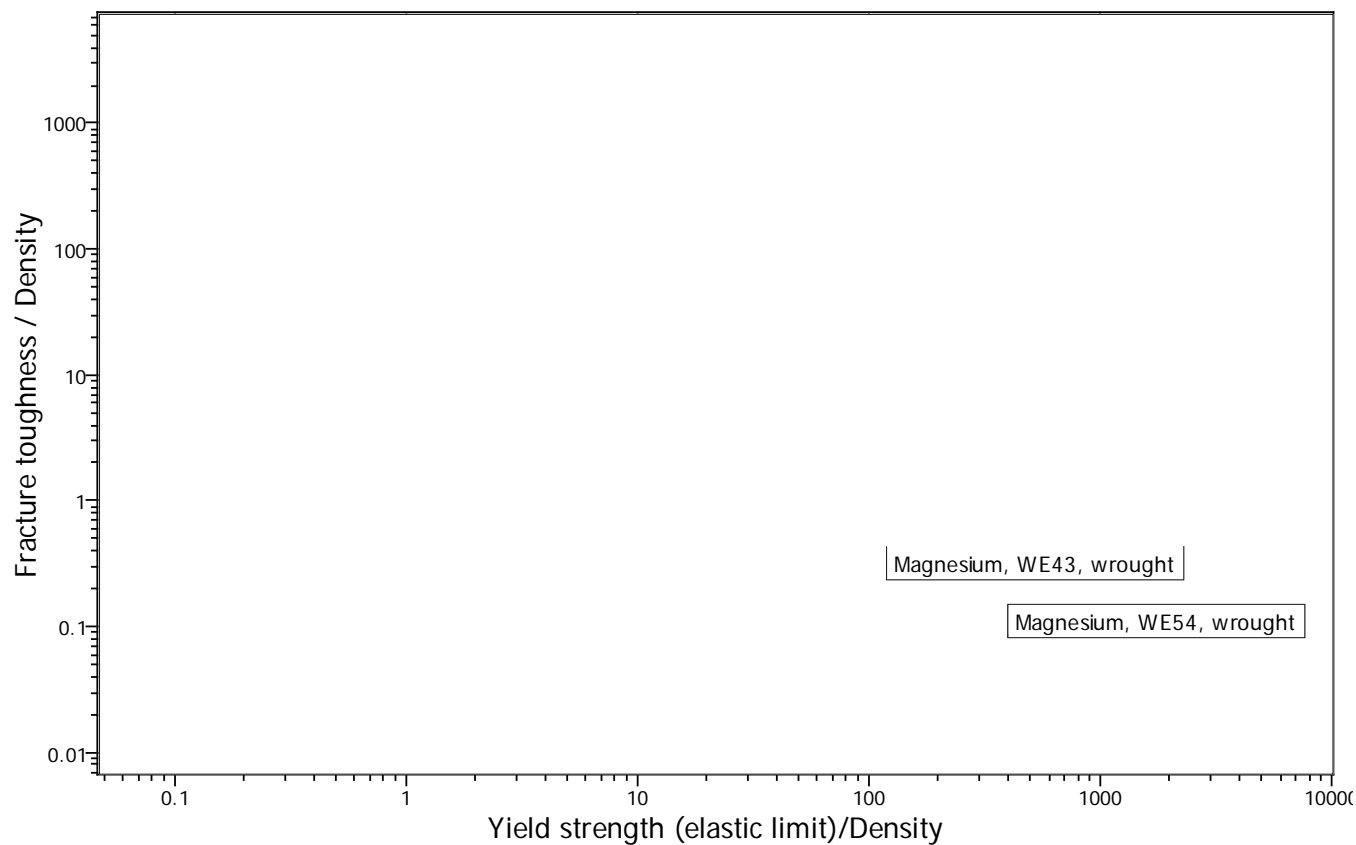
2 System Chart

Figure 6 Magnesium Alloy System Chart

The system chart [8] above illustrates the reciprocity that enables materials engineers to

obtain high performance through the structure design process. Blue boxes and lines indicate foci of this project. To achieve high specific strength and toughness, grain boundary cohesion enhancement is critical. As yttrium in the solid solution of magnesium alloys has been reported as cleavage resistance enhancer, higher yttrium content in the matrix is preferred. Thus part of this work will be the composition design that gives maximal yttrium solubility on the solid solution, which leads to improved matrix ductility. Meanwhile, the strengthening dispersion will be studied with the strengthening model, which describes the relationship of yield strength and phase fraction of precipitates. Details about the model are discussed in a later section. The series of studies will then be organized in a systematic way that ultimately leads to an alloy composition with desired performance.

3   Property Objectives (CES)

Figure 7 CES Plot of Magnesium and Steel Alloys

The Ashby plot above represent two mechanical properties we are interested in for Magnesium alloys: fracture toughness/density vs. yield strength/density. Magnesium alloys, shown in purple, are very appealing to many designers due to their comparable fracture toughness, hardness, and yield strengths to that of steel alloys, shown in green. Current investigation will focus on WE54, which has the potential to have better mechanical properties than WE43.

4   Team Organization

Advisor: Dr. Shengjun Zhang

4.1   Member Profiles

Jie Han

Jie Han is a master student in Materials Science and Engineering. Her interests lie in the modeling and connections of structures and properties. The study on solubility of yttrium in magnesium matrix as a function of temperature appeals to her as it involves clear analysis that rearranges complicated information into logical lines.

Yoon Joo Na

Yoon Joo Na is an undergraduate student pursuing a BS degree in Materials Science and Engineering. She has been working in Professor Jiaxing Huang's research lab for a year as an undergraduate research assistant working on graphene. She is excited to learn about Magnesium alloys and hopes to achieve an improved design using her previous research experience and materials science background knowledge.   She is particularly interested in grain boundary embrittlement and will study Geng's model to find cohesion enhancer elements for magnesium grain boundaries.

 Sky Park

Sky Park is an undergraduate student pursuing a BS degree in Materials Science and Engineering. His previous 6 month co-op experience at GE Aviation exposed him to various nickel, titanium and cobalt superalloys that are currently used at extreme temperatures in jet turbine engines. He examined the γ and γ' microstructure of various turbine engines returned from various airlines to diagnose possible damage due to overheating of the blade. Such microstructural changes require understanding of thermodynamics of the superalloy. For this reason, he is interested in exploring the thermodynamics behind high performance magnesium alloys. An insight into material design of a high temperature alloy, such as Mg WE54, that has the potential to be used in the aerospace industry is a great follow-up to his work experience.

5   Project Organization

RAM Chart

	Han	Na	Park
Background Research	X	X	X
Geng's Model Calculation	X	X	X
Geng's Model Recalibration		X	
Thermodynamic Calculation and Prediction		X	X
Strength Model Calibration	X		X
Hardness Analysis	X		X
Solubility Improvement	X		X
Segregation study	X		
Cooling Analysis	X		
Final Report/Presentation	X	X	X

Gantt Chart

	Apr. 9	Apr. 16	Apr. 23	Apr. 30	May 7	May 14	May 21	May 28
Literature research	X	X	X					

Geng's model calculation			X	X				
Geng's model recalibration			X	X	X	X		
Thermo calculation and prediction				X	X	X		
Strength model calibration				X	X	X		
Solubility improvement and segregation study				X	X	X	X	
Cooling analysis						X	X	
Pre-proposal	X	X						
Proposal				X	X	X		
Final deliverable					X	X	X	X

6   Objectives and Goals

The development of high performance magnesium alloys continues. As illustrated before, magnesium WE43 is the currently most successful commercial Mg alloy. The newly developed magnesium alloy, WE54, can potentially achieve higher strength, but with higher brittleness as well. The goal for this project is to assist the study of magnesium alloys, especially in terms of toughness, that outperforms WE43. Based on Dr. Shengjun Zhang's research and expertise and previous work of MSE 390 students at Northwestern University, three objectives are identified: 1) to improve the grain boundary cohesion with further calibrated Geng's model; 2) to enhance the cleavage resistance by increasing the fraction of yttrium in solid solution; 3) to maximize the strengthening phase that can be precipitated.

7   Approaches and Results

7.1   Grain boundary cohesion

The previous MSE 390 group modeled and predicted grain boundary embrittlement behavior of different solutes using DFT calculations and a phenomenological model. This year, the phenomenological model, specifically the Geng's model, will be recalibrated using more accurately calculated embrittlement potency data on several solute elements

conducted by Dr. Zhang. Equipped with the model, embrittlement potency of other elements in the periodic table can be estimated.

7.1.1 Embrittlement Potency (ΔE)

It has been found that a brittle fracture along the grain boundary has been the primary cause for failure in magnesium alloys. To improve toughness and ductility and to prevent fracture along grain boundaries, various solute elements can be used to enhance the grain boundary cohesion of the material.

According to the Rice-Wang model, the embrittlement potency (ΔE) of an element is defined as the difference between the grain boundary segregation energy and the surface segregation energy as shown in following equation.

$$\Delta E = E_{Seg}^{GB} - E_{Seg}^{Sur}$$

If the grain boundary segregation energy of a solute atom is greater than the surface segregation energy, the atom will promote crack propagation as free surface would be created. On the other hand, for a negative embrittlement potency, ΔE, a solute element will resist free surface formation and intergranular cracking and promote grain boundary cohesion.

Embrittlement potencies can be calculated computationally. 2011 MSE 390 students used VASP method to calculate embrittlement potencies. This year, to obtain more accurate values, Dr. Zhang used Full-Potential Linearized Augmented Plane Wave (FLAPW) method and magnesium Σ7(1230)[0001] grain boundary cells. His results for five solute elements are listed in Table 4.

Table 4 FLAPW Calculated Embrittlement Potency

Solute Atom	GB Embrittlement Potency (eV/atom)
Na	0.238
Y	-0.835
Al	-0.233
Zn	-0.202
Li	0.128

According to the Rice-Wang model, some of these solute atoms are cohesion enhancers. The calculated ΔE values range between -0.835 and 0.238 eV/atom. Since Na and Li have

positive potencies, they are mild embrittlers. Y, Al, Zn are all cohesion enhancers whereas Y can be considered as a strong enhancer due to its large negative ΔE value.

7.1.2   Phenomenological Model of Grain Boundary Embrittlement

Not all elements' embrittlement potencies can be calculated affordably because of computational inefficiency; thus, we need a phenomenological model to estimate other solute atoms' behaviors on grain boundaries. Geng et al. [9] developed a phenomenological model in the form below.

$$\Delta E = \alpha(\Delta E_{coh} + \Delta E_{Sol} + \Delta E_{Str}) + \beta\Delta E_{Vol}$$

ΔE is the embrittlement potency of a solute atom, and it is related to ΔE_{coh}, ΔE_{Sol}, ΔE_{Str}, and ΔE_{Vol}. α and β will be fitted with our DFT calculated embrittlement potencies.

ΔE_{coh} is the cohesive energy difference of a solute atom and the matrix material. These values are readily available in the literature. We used the data from *Introduction to Solid State Physics*, Charles Kittel [10].

ΔE_{Sol} is the heat of solution of a solute atom in the matrix in infinite dilution. This value is available using DFT method but the computational effort would be beyond the scope of this project. Meanwhile, Geng et al. suggested a macroscopic atom model to estimate the heat of alloying with a specific concentration c_A

$$\Delta E_{sol}^{A} = (1 - C_A)[1 + 8C_A^2 \times (1 - C_A)^2] \times \Delta E_{sol}^{A}(0)$$

where
$$C_A = \frac{c_A(V_A)^{2/3}}{c_A(V_A)^{2/3} + (1 - c_A) \times (V_M)^{2/3}}$$

$\Delta E_{sol}^{A}(0)$ is the heat of solution of A in M in infinite dilution, and can be calculated using CALPHAD and SSOL2 and COST database. For very dilute solution, c_A is so small that $\Delta E_{sol}^{A} \approx \Delta E_{sol}^{A}(0)$. Therefore we will use $\Delta E_{sol}^{A}(0)$ for ΔE_{sol}^{A} at this time.

Assume the dilute solution has a composition of $Mg_{0.999}A_{0.001}$, where A denotes the solute, and the formation heat for the alloy is

$$\Delta E_{sol}^{A} = E_{Mg_{0.999}A_{0.001}}^{M} - 0.001E_{A_{0.001}}^{M} - 0.999E_{Mg_{0.999}}^{M}$$

ΔE_{Str} is the total energy difference of crystal A between its stable phase structure and that of the host. We will use data from Y. Wang, et al. [11], who calculated the total energy of

elements in bcc, fcc and hcp lattice. For elements whose stable phases are not bcc, fcc or hcp, their E_{Str} are not readily available and thus not included in our calculation and prediction.

ΔE_{Vol} denotes the volume elastic effect of a substitutional addition solute A in the grain boundary core site. It is consisted of E_{Vol}^M, the elastic energy of matrix, and E_{Vol}^A, the elastic energy of solute A.

$$\Delta E_{Vol}^A = E_{Vol}^A - E_{Vol}^M$$

$$E_{Vol}^A = \frac{2K_A G_M (V^A - V^M - \frac{2}{3}V^{GB})^2}{3K_A V^M + 4G_M V^A}$$

$$E_{Vol}^M = \frac{8K_A G_M (V^{GB})^2}{27K_A V^M + 36G_M V^A}$$

where K_A is the bulk modulus of solute A, G_M is the shear modulus of the matrix, V^A is the volume of atom A, V^M is the volume of the matrix atom, and V^{GB} is the grain boundary free volume. Geng et al. found that V^{GB} for $\sum 3(111)$ boundary in bcc Fe and $\sum 5(201)$ in fcc Ni was 35% and 25% of their bulk values, respectively. For magnesium alloy, we were able to calculate V^{GB} using Dr. Zhang's Mg GB FLAPW model. We found that V^{GB} of Mg was 9.585Å^3, which is about 40% of the bulk value. All other parameters were obtained from literature[12].

7.1.3 Geng's Model
Geng's model was derived for Fe and Ni systems, and it follows the form of

$$\Delta E = \frac{1}{3}(\Delta E_{coh} + \Delta E_{Sol} + \Delta E_{Str}) + \Delta E_{Vol}$$

We will apply this model to the magnesium alloy and test whether this model works for magnesium. If obtained embrittlement potencies are different from DFT calculated values, we will assume that the model coefficients, α and β, are different and recalibrate the model.

2011 MSE390 group recalibrated the equation and came up with following equation.

$$\Delta E = (0.30)\,\Delta E_{coh} + (0.23)\,\Delta E_{Sol} + (0)\Delta E_{Str} + (0)\Delta E_{Vol}$$

Using this model, they claimed that elements in groups 2-5, especially Hf, Ta, and W, can provide the strongest cohesion enhancement. However, this model is very inaccurate

because it does not follow the right form the Geng et al. suggested and ignores structure and volume effects.

This year, given more reliable embrittlement potency values provided by Dr. Zhang (Table 4), we will better recalibrate the Geng's model, and use it to obtain more accurate prediction for the embrittlement potencies of elements in periodic table.

7.1.4 Application of the Original Geng's Model

First, using the original Geng's model for Fe and Ni systems and obtained energy values, ΔE_{coh}, ΔE_{Sol}, ΔE_{Str}, and ΔE_{Vol}, we calculated embrittlement potencies of Na, Y, Al, Zn, and Li and compared with the data calculated by Dr. Zhang. Energy values and compared embrittlement potencies are listed in Table 5.

Table 5 Compared Embrittlement Potency Values of Original Geng's Model and DFT Calculated

Element	ΔE_{coh} (eV/atom)	ΔE_{Sol} (eV/atom)	ΔE_{Str} (eV/atom)	ΔE_{Vol} (eV/atom)	ΔE Geng's	ΔE DFT
Na	-0.397	-1.08e-6	-0.001	0.01795	-0.115	0.238
Y	2.86	-4.77e-16	0	-0.0560	0.897	-0.835
Al	1.88	9.80e-5	0.0295	0.3604	0.997	-0.233
Zn	-0.16	5.66e-15	0	0.4593	0.406	-0.202
Li	0.12	-1.6e-6	-0.0031	0.0352	0.00742	0.128

We found that the embrittlement potencies using the original Geng's model do not match with DFT calculated embrittlement potencies as shown in Figure 8. For example, Y was considered as a strong cohesion enhancer with DFT calculation, but with Geng's model it is considered as an embrittler. Same thing applies for Al. Therefore, we cannot apply the original Geng's model to magnesium system. Because of this discrepancy, the revised Geng's model will be used instead of the original model to estimate embrittlement potencies for other elements.
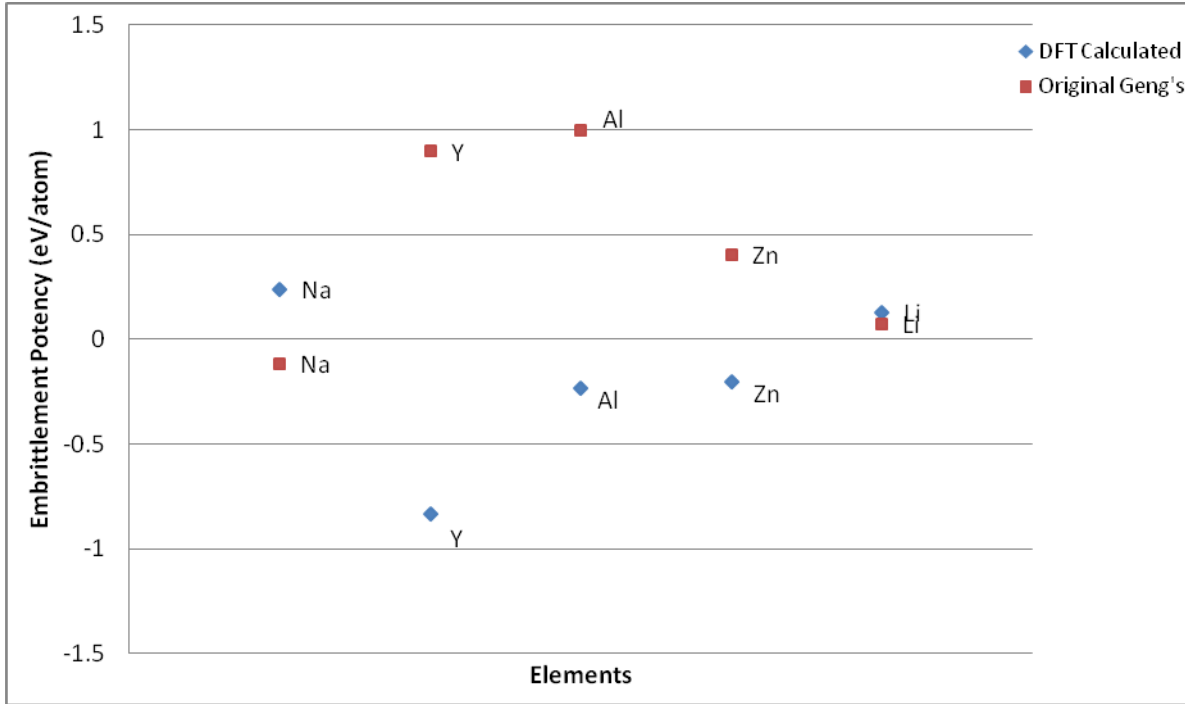
Figure 8 Application of Original Geng's Model

7.1.5

7.1.6 Geng's Model Recalibration and Prediction

Using DFT calculated embrittlement potency values for Na, Y, Al, Zn, Li and obtained energy values, ΔE_{coh}, ΔE_{Sol}, ΔE_{Str}, and ΔE_{Vol}, we estimated parameters of the Geng's model by fitting the parameters. We obtained a well fit result with α =-0.2816 and β=0.887. As shown in Figure 9, we can see that our recalibrated Geng's model matches reasonably with DFT calculated embrittlement potencies except Zn (error of 0.65). However, since it is hard to find alpha and beta parameters that satisfy all six elements, we will continue with these parameters that fit other five elements quite well. Therefore, we will use the following equation to predict embrittlement potency values for other elements.

$$\Delta E = -0.2816(\Delta E_{coh} + \Delta E_{Sol} + \Delta E_{Str}) + 0.887\Delta E_{Vol}$$

We gathered energy values for other elements and estimated the embrittlement potencies using the recalibrated Geng's model. Energy values we used to calculate are tabulated in Appendix A. As shown in Figure 12, we plotted embrittlement potency versus elemental groups in the periodic table and compared it to the figures in Geng's paper as shown in Figure 11. Our recalibrated Geng's model exhibits similar trend as the original Geng's model. The graphs show parabolic trends where embrittlement potencies become positive at the ends of the parabola. Similar to Geng's results for iron and nickel systems, our result for

magnesium system shows that the elements with the most negative potencies are those in group 5 and 6.
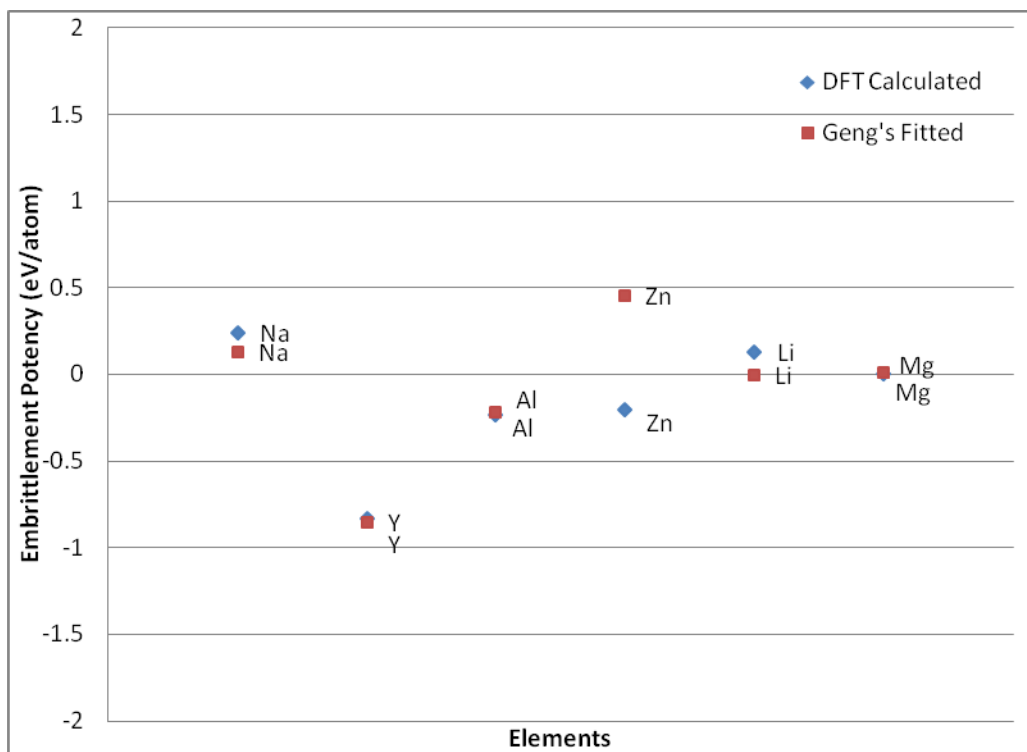

Figure 9 Calibration of Geng's Model
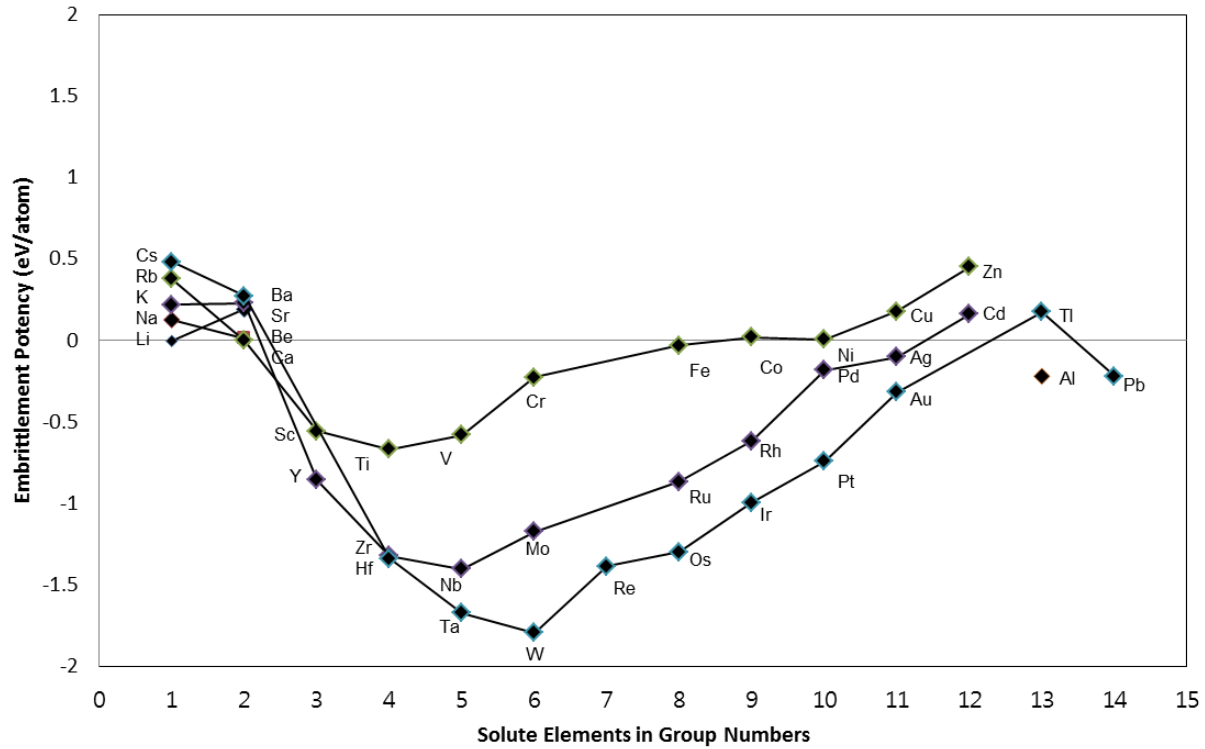
Figure 10 Embrittlement Potency Prediction in Magnesium System

Figure 11 Embrittlement Potency Prediction in Iron and Nickel Systems

Figure 12 shows estimated embrittlement potency values in a periodic table for many elements whose DFT calculations are not available. Elements colored in green have negative embrittlement potency values which indicate that they are cohesion enhancers. Elements in red are embrittlers and are not good for magnesium's grain boundary cohesion.

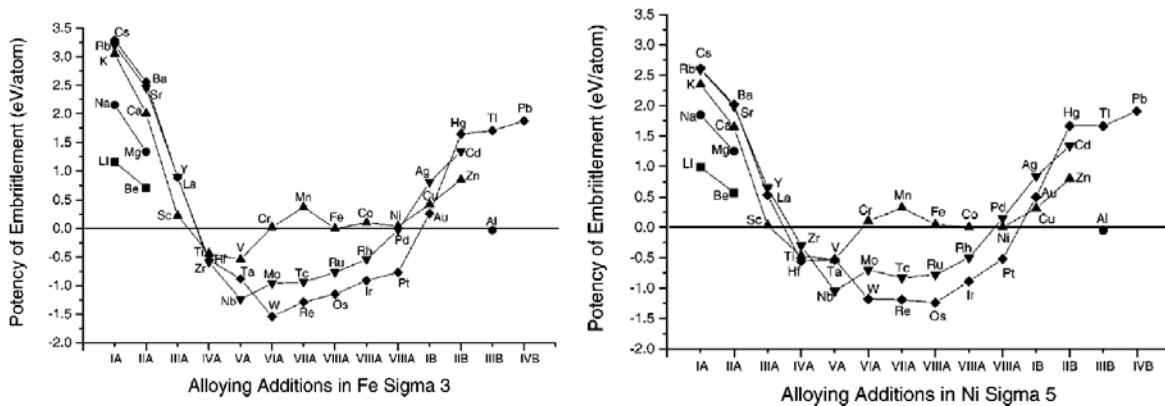Figure 12 Predicted Embrittlement Potency with calibrated Geng's model

Group IA, IIA, and IIB elements are embrittlers because they have positive embrittlement potencies. Group IIB, IVB, VB, VIB, and VIIB elements have negative embrittlement potencies, so they are estimated to be cohesion enhancers. Elements having embrittlement potency values close to zero would not strongly affect grain boundary cohesion. Large magnitude of embrittlement potency would make an element either a strong embrittler or a strong cohesion enhancer depending on the sign.

However, the revised model we obtained has an error of 0.65 in embrittlement potency as mentioned earlier. Therefore, an element with embrittlement potency greater than 0.65 in magnitude is either an embrittler or a cohesion enhancer for sure. These elements are boxed with thicker lines in Figure 12. We already know from literature that zirconium and yttrium are good cohesion enhancers, and our result well matches this fact.

7.2   Solute segregation to the grain boundary

From literature and the discussion above, we know that yttrium and zirconium are good grain boundary cohesion enhancers, and zirconium plays an important role as a grain

refiner as well. Meanwhile, the contents of both elements in the matrix are relatively high. When they accumulate along the grain boundaries, they will pin the grains together and hence improve the cleavage resistance. Therefore, the segregation of Y and Zr to the grain boundaries will influence significantly their actual effects of grain boundary cohesion enhancement.

Langmuir-McLean theory deals with the grain boundary segregation. With basic statistical mechanics, it determines the fractional monolayer of segregant that minimizes the system energy at the equilibrium. The McLean equation is

$$\frac{C_{GB}}{1-C_{GB}} = \frac{C_{Bulk}}{1-C_{Bulk}}\exp(-\frac{E_{GB}}{RT})$$

where C_{Bulk} is the solute concentration in the bulk that is determined by atom probe, C_{GB} the solute concentration in the grain boundaries that we are interested, E_{GB} the segregation energy, T the absolute temperature, and R is the universal gas constant.

As C_{Bulk} is very small and 1- C_{Bulk} ≈1, it is appropriate to use the following equation [15]:

$$\frac{C_{GB}}{1-C_{GB}} = C_{Bulk}\exp(-\frac{E_{GB}}{RT})$$

Using the segregation energy obtained from first principle calculation by Dr. Zhang, we can estimate the concentration in the grain boundaries. Table 6 lists the calculation result. It indicates that both yttrium and zirconium segregate to the grain boundaries at room temperature, which will benefit the grain boundary cohesion.

Table 6 Segregation in the Mg GB

Element	Segregation energy (eV/atom)	Concentration in the bulk (at.%)	Concentration in the GB (at.%)
Y	-0.930	0.59	100
Zr	-0.281	0.18	99

7.3   Precipitation Strengthening

The total yield strength consists of the strength of the magnesium matrix, the strengthening of grain boundary refining, the contribution from solid solution strengthening determined by matrix composition, and the contribution from precipitation strengthening which is controlled by the finely dispersed precipitates:

$$\sigma_y = \sigma_0 + \Delta\sigma_{GB} + \Delta\sigma_{sss} + \Delta\sigma_{ppt}$$

In this work, we will focus on the precipitation strengthening, $\Delta\sigma_{ppt}$, which is a combination of two mechanisms:

Shearing mechanism: $\Delta\sigma_{ppt} = K_1 r^{1/2} f^{1/2}$ (Equation 1)

Orowan mechanism: $\Delta\sigma_{ppt} = K_2 \dfrac{f^{1/2}}{r}$ (Equation 2)

where K_1 and K_2 are constants, r is the radius of the precipitates and f is the volume fraction of the precipitates.
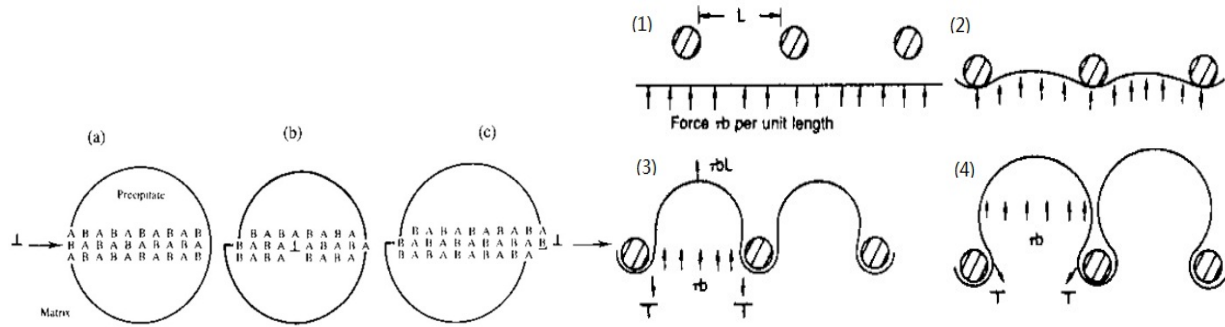

Figure 13 Shearing (left) and Orowan (right) mechanisms [14]

The two models describe the interaction of dislocations and pinning particles as shown in Figure 13. Initially, as precipitates form, the interface between precipitate and matrix phases is coherent and shearing model will dominate. However, as alloy undergoes aging and precipitate particles grow, the interface becomes incoherent and Orowan looping will occur. Both of the mechanisms simultaneously contribute to the strengthening. The Orowan mechanism dominates when the particle radius is small and shearing mechanism gradually takes control as the particle radius increases. Therefore, under a constant phase fraction f, a critical radius which gives maximal strengthening exists.

From the atom probe result (Figure 14), we can calculate the mean volume of the precipitate by treating the particles as cylinders. However, for convenience, we will further assume that the precipitate particles are spherical to obtain the average radius of the particle to be 10.30nm.
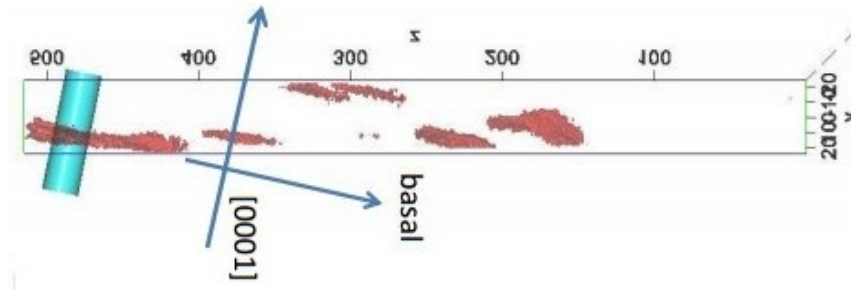
Figure 14 Particles image from atom probe

Using peak hardness and yield strength data from Figure 3 and Figure 20, we can fit the two models in the form of $\Delta\sigma_y = C_1 r^{1/2}$ and $\Delta\sigma_y = \dfrac{C_2}{r}$, where C_1 and C_2 are constants. These two models are similar to Equation 1 and Equation 2 respectively, but the phase fraction f of precipitate is treated to be constant and is absorbed into the constants C_1 and C_2. Figure 15 shows the fitted curves. The intersecting points are the critical radius corresponding to optimal yield strength and hardness. Since we have only one data point, the critical radius will be the precipitate radius of the WE43 atom probe sample at peak hardness, 10.30nm.

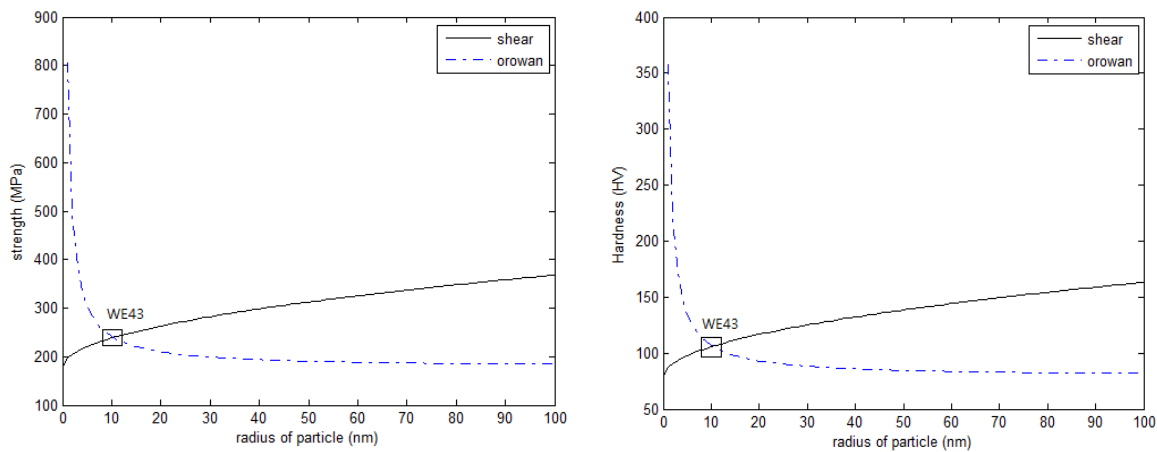Figure 15 Critical radius for peak yield strength (left) and hardness (right)

The precipitation amount also influences the precipitation strengthening. For a given particle radius, both shearing and Orowan models give the relation $\Delta\sigma_y = Bf^{1/2}$ where B is constant. By fitting this model with known WE43 data, we will be able to make strengthening predictions with respect to precipitate phase fraction.

The phase fraction of precipitates can be determined from atom probe results by Dr. Zhang (Table 7).

Table 7 Atom probe results after 8h ageing from Dr. Zhang

at.%	Mg	Y	Zr	Ga	Nd	Gd	Dy	Zn
Matrix	98.09	0.96	0.27	0.12	0.26	0.14	0.07	0.09
Precipitate	87.58	3.06	0.79	0.18	4.09	0.56	0.19	0.12

Since this work will utilize the Mg-Y-Nd ternary system, the atom probe data must be simplified. As the precipitation temperature for β'' is below 200°C, the precipitate at 250°C is most likely to be β' or β phase. The composition for β' and β in WE43 has been reported to be $Mg_{12}NdY$ and $Mg_{14}Nd_2Y$, respectively [13]. However, for more accurate analysis, we will adopt Nd:Y ratio from Dr.Zhang's atom probe results. Meanwhile, because there are phase overlaps, the magnesium content is overestimated for precipitates. Therefore, we will use the Mg:Nd ratio from literature, which is 12:1 for β' phase. As we focus on Mg-Y-Nd ternary system, impurities will be adjusted and merged into yttrium and neodymium contents, as listed in Table 8. Meanwhile, the initial alloy (WE43) composition in at.% is $Mg_{98.25}Nd_{0.59}Y_{1.16}$.

Table 8 Adjusted Compositions

	Element	Mg	Y	Nd
wt.%	Matrix	92.53	5.17	2.30
	precipitate	58.03	13.27	28.70
at.%	Matrix	98.09	1.5	0.41
	precipitate	87.27	5.45	7.27

Figure 16 shows the ternary diagram plotted with the Mg-Y-Nd database revised by Dr. Zhang at aging temperature of 250°C with labels of different phase regions. Figure 17 is a detailed view of the low Nd and Y mole fraction region of the system.

Figure 16 Ternary diagram at 250°C
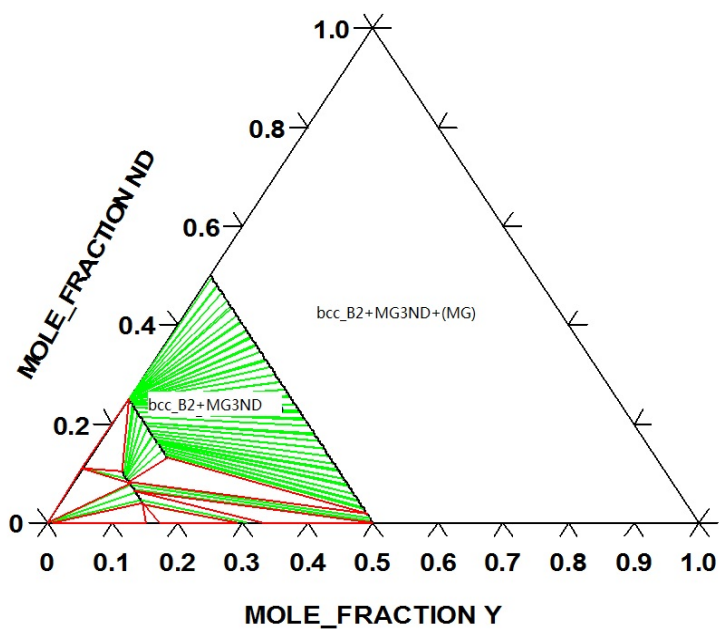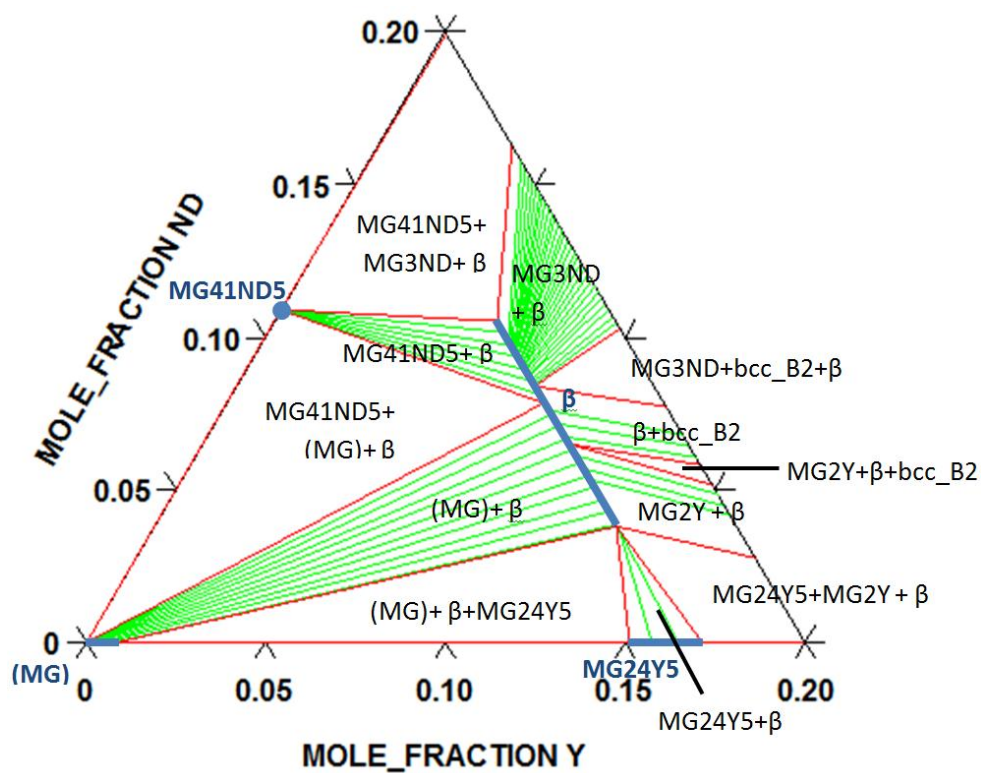

Figure 17 The Mg-Y-Nd isothermal section at 250°C

Figure 18 and Figure 19 mark the initial matrix (1), precipitate (2) and alloy (3) composition in the ternary phase diagram. Figure 18 exhibits the complete triangle diagram, while Figure 19 is the magnified view of the region of interest.
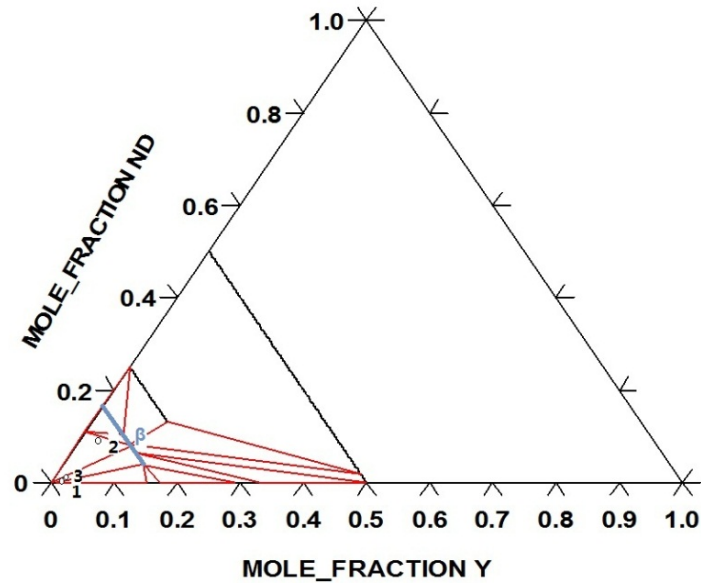

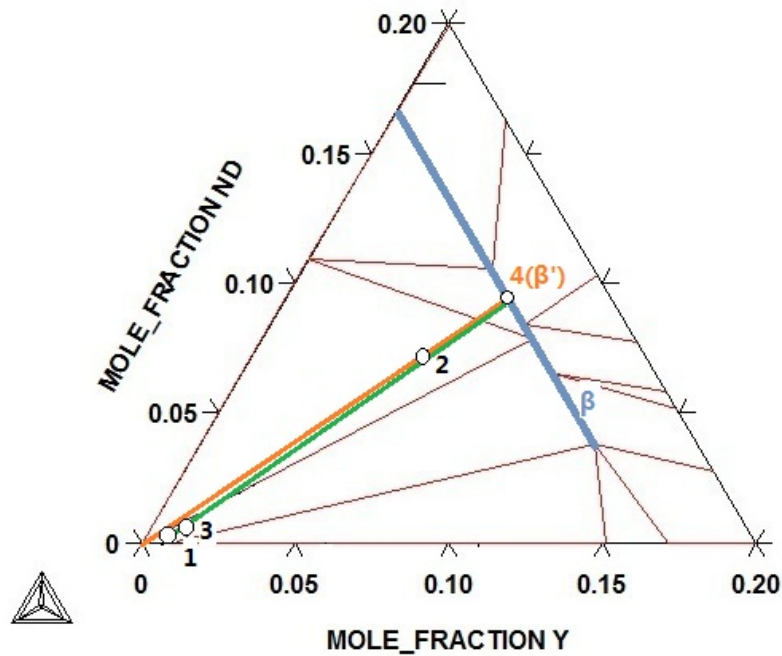Figure 18 Matrix, precipitates and alloy composition points

Figure 19 Precipitate composition

We find that the WE43 alloy composition lies at the edge of the two phase region of hcp Mg and β. According to atom probe results, the matrix composition after aging stays in the same region, while the precipitate falls into the hcp-β-$Mg_{41}Nd_5$ three phase region. This is because the precipitate phase β' is metastable and thus not labeled in the equilibrium ternary phase diagram.

The metastable β' phase plays important role in precipitation strengthening. Meanwhile, the precipitate composition detected by atom probe may not be pure β', but an intermediate composition that will evolve to β' point in later stage. We can use this intermediate composition to estimate the composition of β'. We assume that in the isothermal diagram, β' phase line is close to the line of β phase, which is marked with blue in both figures. Connect the precipitate point with the pure magnesium corner using a straight line, and extrapolate it to intercept with β' phase line, as shown by the orange line in Figure 19. We can then read the composition of β' phase at point 4. The composition is $Mg_{83.46}Nd_{9.27}Y_{7.27}$.

Connect β' (4) and matrix (1), and we obtain the tie line of the two phases (green line in Figure 19). Theoretically, the initial alloy (3) composition should lie in the tie line. However, slight deviation exits, so we treat the projection of (3) to the tie line as the alloy composition in the following calculation. With lever rule, the phase fraction of β' is estimated to be 1.65%.

Strengthening model for yield strength

Figure 20 is the stress-strain curve of the tensile test for WE43. We can read from the curve the 0.2% proof strength of the sample before and after 8 h aging.
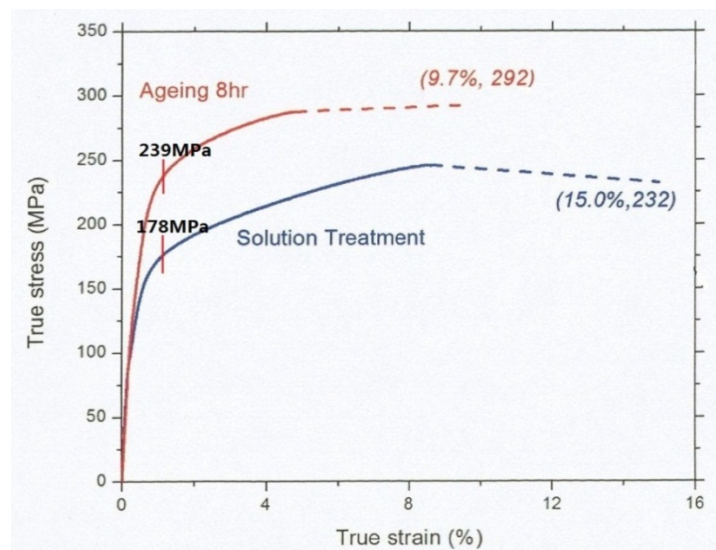
Figure 20 Stress-Strain curve for WE43 from Dr. Zhang

As the yield strengths before and after aging are 178MPa and 239MPa, respectively. The contribution of precipitation strengthening is 61MPa. To fit the strengthening model versus the phase fraction of precipitates, the constant B=475, and the curve is plotted in Figure 21.
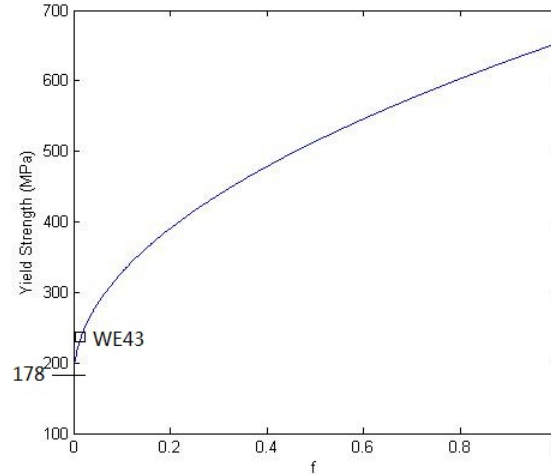
Figure 21 Strength model

Given the calibrated strengthening model, we can estimate how much we can increase the yield strength by improving the phase fraction of precipitates.

Strengthening model for peak hardness

The peak hardness also appears after 8 h aging. With hardness data from Dr. Zhang (Figure 3), we can calibrate the strengthening model again using the peak hardness. The hardness before age treatment is 79HV, thus the contribution of precipitation strengthening is 27HV. The model coefficient B is then 210. Figure 22 illustrates the calibrated strength curve for peak hardness.
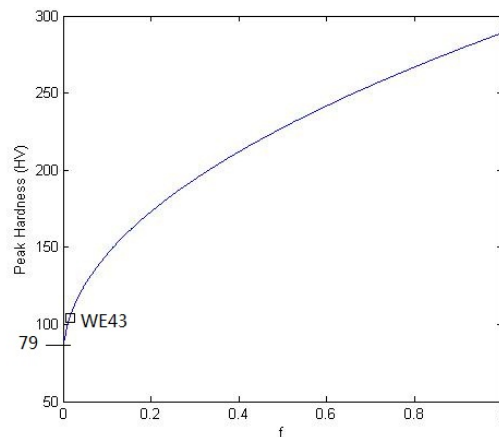
Figure 22 Strength model (for peak hardness)

Change in composition with elongated aging time

If we age for more than 8 hours, the precipitate composition will change, as shown in Table 9.

Table 9 Atom probe after 16h aging from Dr. Zhang

at.%	Mg	Y	Zr	Ga	Nd	Gd	Dy	Zn
Matrix	98.61	0.59	0.18	0.18	0.17	0.14	0.04	0.09
Precipitate	87.58	1.88	3.10	0.29	5.78	0.89	0.31	0.16

Comparing the result for 16 hour aging and that for 8 hour aging, the sample after only 8 hour heat treatment has less amount of precipitation. Also, we can find that as aging time increases, Nd content in precipitates (β' phase) increases, while the amount of Y decreases. The Nd:Y ratio after 8 hour aging is about 4:3; after 16 hour, Nd:Y=3:1. One possible explanation is that with longer aging time, the metastable β' phase transforms gradually to stable β phase, which is reported to have Nd:Y=2:1[3]. Though 16 hour aging is more common in industrial manufacturing, the experiment results indicate that the peak value occurs after 8 hour aging. Therefore, our emphasis will be on the sample prepared under the aging treatment condition of 250°C for 8 hours.

7.4 Yttrium solubility

In magnesium alloys, yttrium is important to strengthening and matrix ductility. It also forms precipitates according to the reaction

$$xMg + yY + zNd \rightarrow Mg_x Y_y Nd_z$$
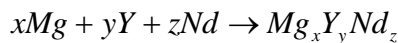
$Mg_x Y_y Nd_z$ precipitates to introduce precipitation strengthening, while a small amount of yttrium remains in the solid solution and contributes to the improved cleavage resistance. The higher fracture toughness, therefore, is promoted with higher fraction of yttrium in the solution. Strategy for this is to study yttrium's solubility in the matrix in equilibrium with precipitated β' phase, whose composition has been calculated above to be $Mg_{83.46}Nd_{9.27}Y_{7.27}$.

The precipitation amount acts as one constraint. A certain phase fraction of precipitated particles is required to maintain peak hardness. Hence the ratio of β' phase to the matrix phase α should be fixed. The vertical section constructed along the tie lines connecting β' and α phase in the Mg-Y-Nd ternary phase diagram will be used to estimate the maximum amount of yttrium soluble in the matrix, $X_{Y, MAX}$, and corresponding neodymium concentration $X_{Nd, MAX}$, under the aging temperature (250°C) which is used by MEL Ltd., company in producing Elektron WE54 and WE43.

It is then possible to calculate the solubility product K_S and build the temperature dependence of yttrium's solubility with it. For a system $Mg_XY_YNd_Z$ where $X_{Mg} \approx 1$, the solubility product K_S can be expressed as:

$$\ln K_S = \ln X_{Mg}^{x} X_{Nd}^{y} X_{Y}^{z} = \frac{\Delta G_{f}^{O}}{RT} - \ln \gamma_{Mg}^{x} \gamma_{Y}^{y} \gamma_{Nd}^{z}$$

This expression connects X_Y and T. In manufacturing commercial WE54 and WE43, a solution temperature of 525°C is used. Calibrating with the solution temperature of WE43, we can extrapolate to obtain the solvus line in the vertical section of the ternary phase diagram. The maximal solubility of yttrium and corresponding temperature can be identified by overlaying the solvus with solidus in the vertical section diagram, and we will be able to identify the corresponding alloy composition. Figure 23 shows the vertical section along the tie line that connects the β' ($Mg_{83.46}Nd_{9.27}Y_{7.27}$) and pure magnesium, which is the orange line in Figure 19. As the ratio of Nd and Y should be maintained as constant, the X axis cannot reach 1, so we set it from 0 to 0.25. Figure 24 shows the magnified region of interest.
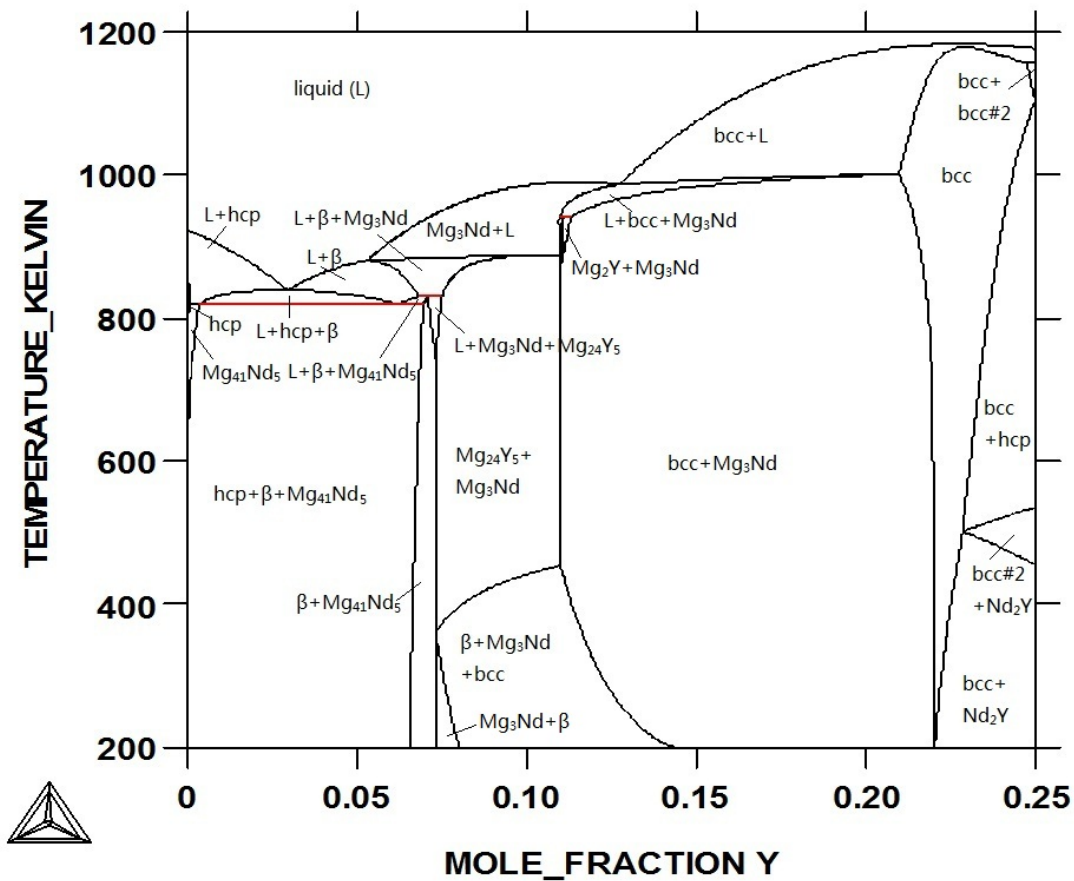

Figure 23 The vertical section across the precipitate composition

As we did in yield strength model calibration, the projection of WE43 composition to the tie line (Figure 19) is treated as the nominal composition of the alloy. The nominal point is also marked as the small circle in Figure 24.
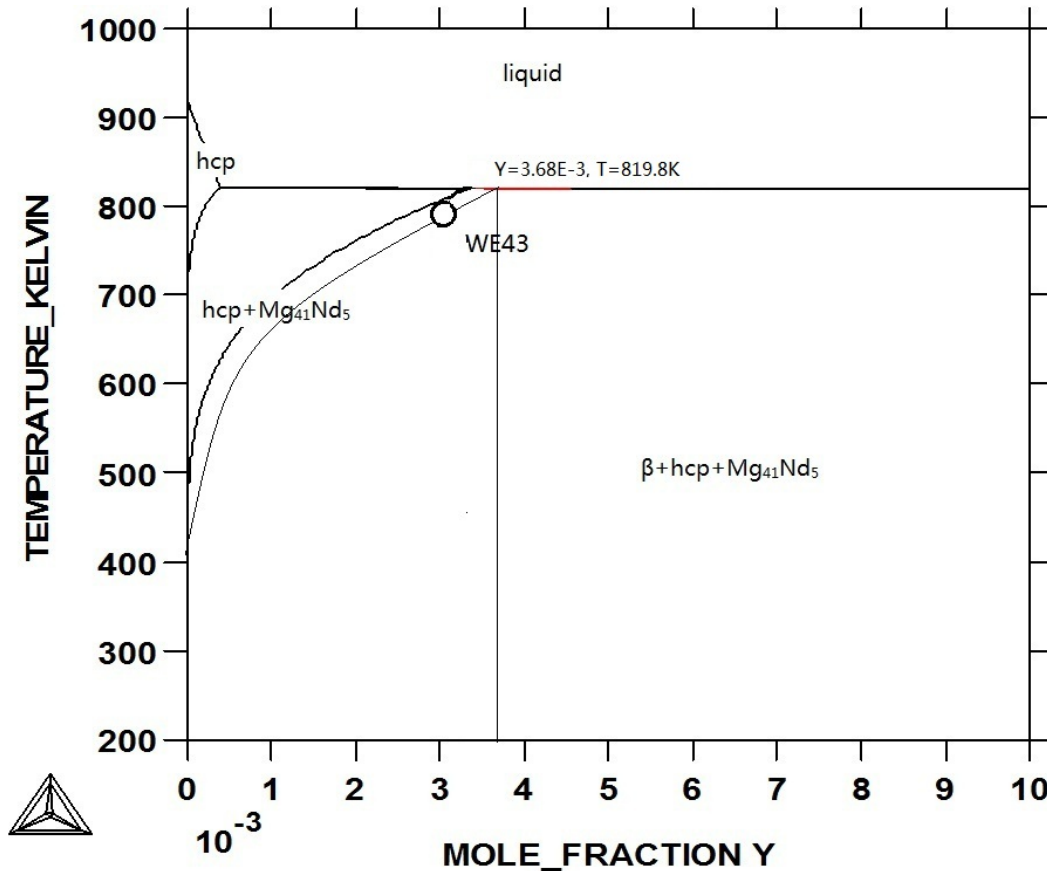
Figure 24 Zoomed vertical section

Theoretically, the WE43 point should lie in the solvus. However, the current database does not contain information about the metastable phase and thus the composition point of the alloy deviates greatly from the solvus of hcp Mg in Figure 24. To obtain good estimation, the database must be modified to fit the WE43 point and to reconstruct the solvus line. Last year's group changed the regular solution model enthalpy of mixing between Mg and Nd in the Mg_hcp phase, and the enthalpy of mixing between Mg, Nd and Y in the β phase. However, this database calibration is not within the scope of this year's work. Therefore, only a rough estimation is made as shown in Figure 24. The projection of alloy composition that gives maximal yttrium solubility can be determined as $Mg_{97.75}Y_{1.41}Nd_{0.84}$ with a solution temperature of 820K. Point 5 in Figure 25 marks the new composition. Using lever rule, its precipitate phase fraction is calculated to be 2.2%. The predicted peak hardness is 110 HV and yield strength is 248MPa, which are not significantly improved compared with the peak hardness (106HV) and yield strength (239MPa) of WE43 according to Dr. Zhang's measurements. Figure 26 plots the predicted yield strength for this alloy composition.
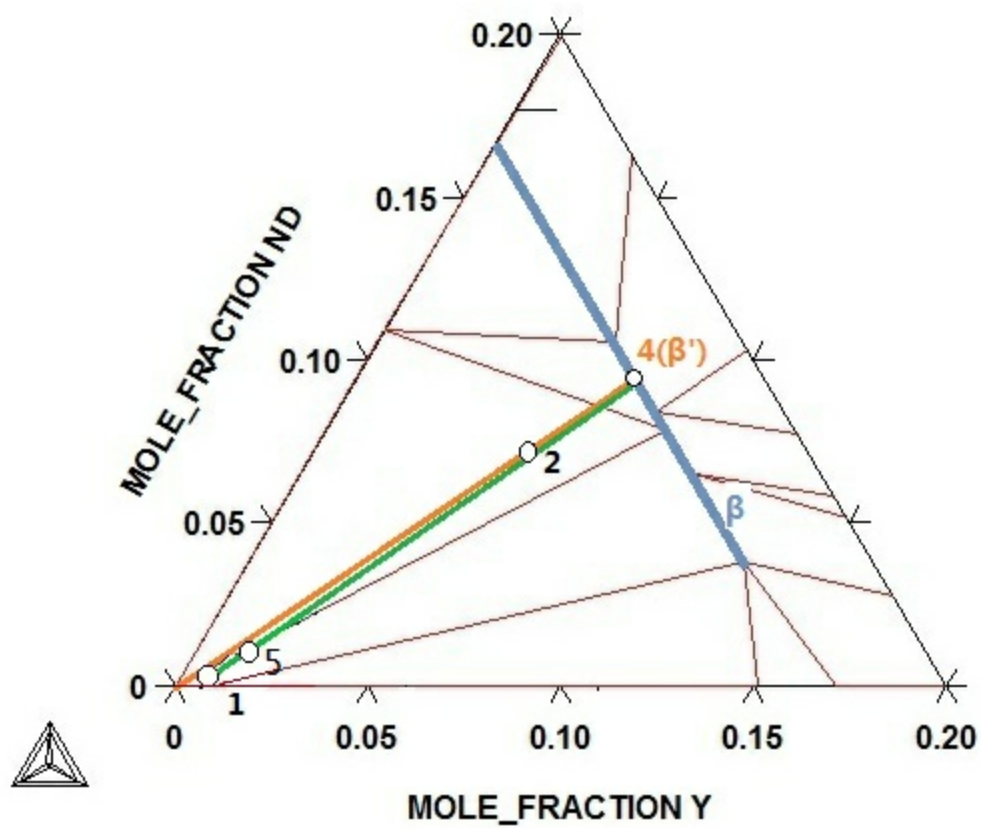
Figure 25 Estimated optimal alloy composition
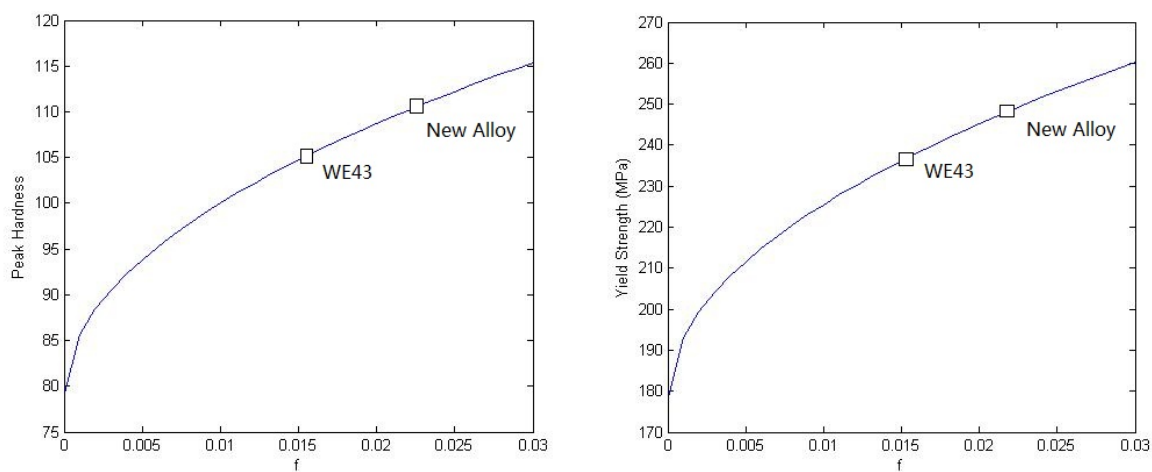
Figure 26 Predicted peak hardness (left) and yield strength (right) of the new alloy

The new alloy does not show significantly improved strength compared with WE43, but we expect it to have better ductility because the yttrium content is higher.

7.5 Cooling analysis

To analyze the evolution of phases during the cooling process at the precipitate composition detected by the atom probe of Dr. Zhang, the cooling curve portraying phase fractions versus temperature is plotted in Figure 27, where BPW stands for the normalized mass fraction of the phase. Figure 28 shows the zoomed details. Though we cannot access the metastable phase β', the cooling curve gives the evolution of phase fraction of β, which also contributes to the precipitation strengthening and discloses information of β' as we assume that β' behaves similar to β.

Figure 27 Cooling curve

Figure 28 Details in the cooling curve

The cooling curve provides some reference for processing. We can read that as temperature goes down, the liquid solidifies into hcp matrix at 607°C and starts to precipitate $Mg_{41}Nd_5$ at 520°C. Thus the solution treatment temperature should lie between. The solution temperature currently used in industry is 525°C. It is expected that by increasing it to 550°C, higher precipitation amount can be obtained.

The β phase does not appear until 348°C, when the amount of $Mg_{41}Nd_5$ peaks. Continue cooling down, and the fraction of β phase increases as that of $Mg_{41}Nd_5$ decreases. The maximal amount of β phase (0.64%) is obtained at 134°C. Below that temperature, the fraction of β goes down slightly and ends in around 0.62% at 0°C. For current industrial aging temperature, which is 250°C, the possible fraction of β precipitates will be 0.55%. Lower the aging temperature can increase the amount of β phase.
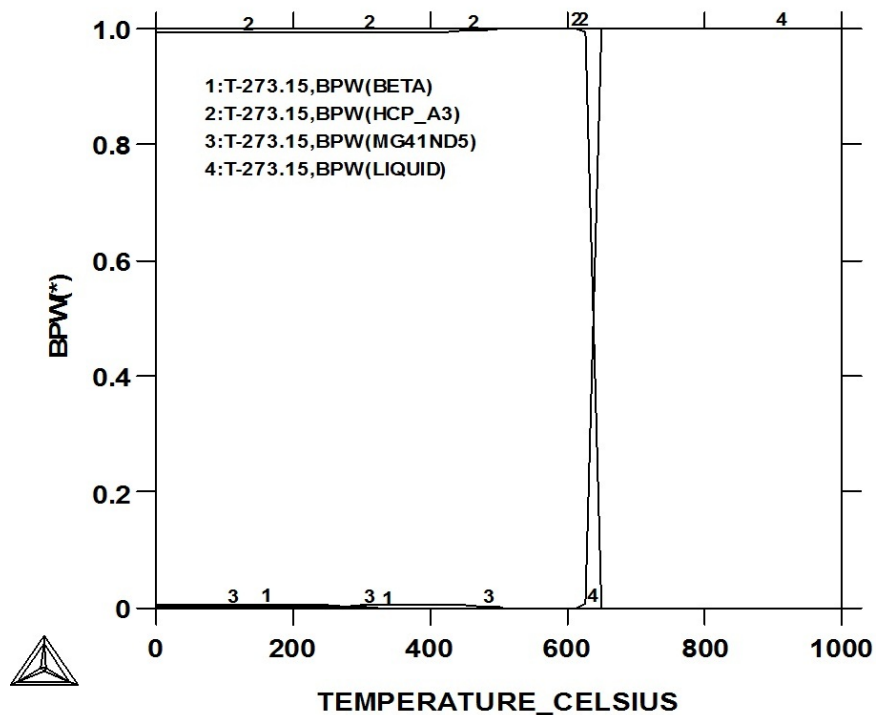
8   Conclusion

1. In order to study behaviors of various solute elements in magnesium grain boundaries, we came up with a phenomenological model. Using revised Geng's model, we estimated embrittlement potency values for elements whose DFT calculations were not available. We found that group 5 and 6 elements have the most negative potency values. We concluded that following elements are cohesion enhancers: Ti, Y, Zr, Nb, Mo, Ru, Hf, Ta, W, Re, O

 2. According to McLean equation, yttrium and zirconium will segregate to the grain boundary and thus contribute to the grain boundary cohesion significantly.

3. According to atom probe data, the precipitate phase fraction of WE43 is 1.65%, and the calibrated strengthening model is $\sigma_y = 178 + 475 f^{1/2}$ for yield strength and $\sigma_y = 79 + 210 f^{1/2}$ for peak hardness.

4. The composition corresponding to maximal yttrium solubility is roughly estimated to be $Mg_{98.03}Y_{1.43}Nd_{0.54}$ with the solution temperature of 820K. Its yield strength is 248MPa, which is higher than the experimental result of WE43 (239MPa).

5. Cooling analysis indicates that higher precipitation amount may be achieved by increasing the solution temperature to 550°C. At current aging temperature, 250°C, and at the precipitate composition, the maximal phase fraction of β is 0.55%. Lowering the aging temperature   may   increase   the   phase   fraction   of   β.

Reference

[1] Magnesium Elektron datasheet for Elektron WE43 and Elektron WE54

[2] T. Rzychon, A. Kielbus, B. Biers, Characterization of β Phase in WE54 Magnesium Alloy, Solid State Phenomena, 2007, 130: pp. 155-158

[3] N. Zaludova, Mg-RE Alloys and Their Applications, WDS'05 Proceedings of Contributed Papers, 2005, Part III: pp. 643-648

[4] Nie J. F., Muddle B.C., Precipitation in Magnesium Alloy WE54 During Isothermal Aging at 250℃, Scripta Materialia, 1999, 40 (10): pp. 1089-1094

[5] T. Rzychon, J. Michalska, A. Kielbus, Corrosion Resistance of Mg-RE-Zr Alloys, Journal of Achievements in Materials and Manufacturing Engineering, 2007, 21(1): pp. 51-54

[6] A. Kielbus, The Influence of Aging on Structure and Mechanical Properties of WE54 Alloy, Journal of Achievements in Materials and Manufacturing Engineering, 2007, 23(2): pp. 27-30

[7] B. Smola, et al., Microstructure, Corrosion Resistance and Cytocompatibility of Mg-5Y-4Rare Earth-0.5Zr (WE54) Alloy, Materials Science and Engineering C 32, 2012, pp.659-664

[8] M. Chen, A. Counts, J. Doak, High Performance Magnesium Final Report, 2011, MSE 390 course project.

[9] W. T. Geng, A. J. Freeman, G. B. Olson, Influence of Alloying Additions on Grain Boundary Cohesion of Transition Metals: First-Principles Determination and Its Phenomenological Extension, Physical Review B, 2011, Volume 63, 165415

[10] Charles Kittel, Introduction to solid state physics (8th ed), 2005, John Wiley & Sons, Inc, ISBN 0-471-41526-X, pp.50

[11] Y. Wang, et al. Ab initio lattice stability in comparison with CALPHAD lattice stability, Computer Coupling of Phase Diagrams and Thermochemistry, 2004, 28, pp.79-90

[12] F. Cardarelli, Materials Handbook: a concise desktop reference, 2000, Springer, ISBN 1-85233-168-2, Appendices table 15.2a

[13] C. Antion, P. Donnadieu, F. Perrard, A. Deschamps, C. Tassin, A. Pisch, Hardening Precipitation in a Mg-4Y-3RE alloy, Acta Materialia, 2003, 51: pp. 5335-5348

[14] Wole Soboyejo, Mechanical Properties of Engineered Materials, 2002, Marcel Dekker, Inc., ISBN0-8247-8900-8, Chapter 8

[15] Shengjun Zhang, Oleg Y. Kontsevoi, Arthur J. Freeman, Gregory B. Olson, First Principles Investigation of Zinc-induced Embrittlement in an Aluminum Grain Boundary, Acta Materialia, 2011, 59: pp. 6155-6167

9 Appendix A. Estimation of Embrittlement Potencies

Element	Embrittlement potency(eV/atom)	ΔEcoh (eV/atom)[10]	ΔEsol (eV/atom)	ΔEstr (eV/atom) [11]	ΔEvol (eV/atom)[12]
Li	-0.001693858	0.12	-0.0000016	-0.0031	0.035201
Na	0.127996386	-0.397	-0.00000108	-0.001	0.017952
K	0.379782712	-0.576	0.000000519	0.0019	0.245906
Rb	0.220032664	-0.658	0.00000208	-0.0009	0.038887
Cs	0.482738082	-0.706	0.00000519	-0.0019	0.319501
Be	0.192891375	1.81	-9.13E-15	0	0.792062
Mg	0.013379958	0	-4.56E-09	0	0.015084
Ca	0.00118615	0.33	0.00000519	0.003	0.107053
Sr	0.229248482	0.21	0.0000026	0.0039	0.326355
Ba	0.272316991	0.39	0.0000208	0.0127	0.434852
Sc	-0.554450901	1.88	-2.8E-15	0	-0.02825
Y	-0.855047063	2.86	-4.98E-15	0	-0.05603
La	N/A	2.96	0.0000253	N/A	0.016702
Ti	-0.667568148	3.34	-8.28E-16	0	0.30771
Zr	-1.319126444	4.74	-8E-15	0	0.017599
Hf	-1.338082601	4.93	-1.27E-15	0	0.056545
V	-0.578740422	3.8	0.0000415	0.2537	0.634436
Nb	-1.400337547	6.06	0.000104	0.2915	0.437661
Ta	-1.669169798	6.59	0.0000188	0.2779	0.298493
Cr	-0.225871473	2.59	0.0000462	0.3904	0.691526
Mo	-1.172210254	5.31	0.0000812	0.4133	0.495412
W	-1.791639466	7.39	0.000153	0.4853	0.480274
Mn	N/A	1.41	0.0000402	N/A	0.780442
Re	-1.38447237	6.52	-6.61E-15	0	0.509005
Fe	-0.029481185	2.77	0.0000595	0.0072	0.848429
Ru	-0.866133803	5.23	1.04E-15	0	0.683848
Os	-1.29751962	6.66	1.1E-15	0	0.651478
Co	0.021767995	2.88	0.0000885	0	0.93885
Rh	-0.615358524	4.24	0.0000173	0.0338	0.663018
Ir	-0.992934656	5.43	0.0000415	0.0679	0.625956
Ni	0.007037517	2.93	0.00003	0.0221	0.945113
Pd	-0.179962543	2.38	0.0000208	0.0259	0.560894
Pt	-0.740977049	4.33	0.000026	0	0.539242
Cu	0.178529568	1.98	-0.000297	0.0054	0.831459
Ag	-0.100008791	1.44	0.00000311	0.003	0.345346

Au	-0.315378604	2.3	0.0000025	0.0008	0.374858
Zn	0.452448582	-0.16	-5.66E-15	0	0.459288
Cd	0.162923988	-0.35	-1.25E-15	0	0.072567
B	N/A	4.3	1.18E-15	N/A	1.434163
Al	-0.217976162	1.88	0.000098	0.0295	0.360477
Tl	0.176007745	0.37	1.14E-15	0	0.315887
C	N/A	5.86	-5.29E-10	N/A	1.001763
Si	N/A	3.12	-0.000824	N/A	0.159891
Sn	N/A	1.63	-0.000701	N/A	-0.06371
Pb	-0.218446092	0.52	-4.56E-09	0.0187	-0.07526